Spatial patterns and possible mechanisms of precipitation changes in recent decades over the Tibetan Plateau in the context of intense warming and weakening winds

xiaoyu Guo[1] and Lide Tian[2]

[1]Institute of Tibetan Plateau Research, Chinese Academy of Sciences
[2]Institute of International Rivers and Eco-security, Yunnan University

November 24, 2022

Abstract

The Tibetan Plateau (TP) significantly affects its surroundings and the global climate through thermal and dynamic processes. Precipitation is a key driver of hydrological, meteorological, and ecological processes. In general, the precipitation over the TP displays a wetting trend over the past half century, with large spatial heterogeneity. However, the causes of such spatially variable trends in TP precipitation and the driving forces have not been well quantified. Here we investigate the spatial variations in precipitation trends and their possible mechanisms, using ground-based observations from 132 CMA (China Meteorological Administration) stations (1970–2016) and CMFD (China Meteorological Forcing Dataset) reanalysis data (1980–2016) over the TP. The major findings are: (1) Pronounced spatial patterns of precipitation changes (increasing on the inner TP and decreasing for regions around the TP) are observed in both CMA and CMFD data. (2) Maximum precipitation decreases generally occurred in stations that experienced a southwesterly daily maximum wind speed (W_s). (3) Positive correlations between mean precipitation amount and corresponding temperature (or W_s) are obtained in directions of maximum precipitation increase (decrease), which are further verified by the qualitative and quantitative analysis of the CMFD dataset. Therefore, we suggest that intensified local recycling in a warming and hydrologically unbalanced environment has led to precipitation increases on the central TP, whereas precipitation decreases in areas bordering the TP may be the result of a weakening Indian monsoon.

Hosted file

`supplements.doc` available at https://authorea.com/users/547205/articles/602675-spatial-patterns-and-possible-mechanisms-of-precipitation-changes-in-recent-decades-over-the-tibetan-plateau-in-the-context-of-intense-warming-and-weakening-winds

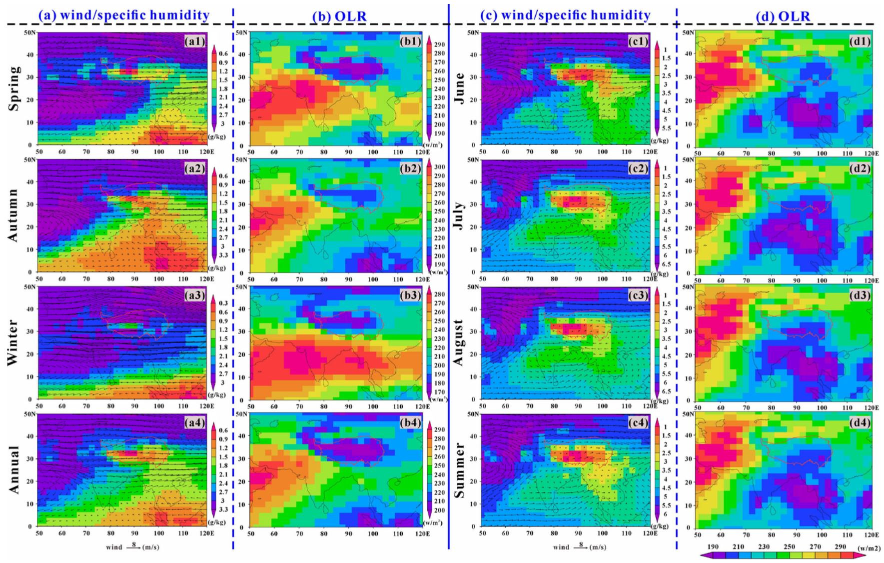
(a) wind/specific humidity
(b) OLR
(c) wind/specific humidity
(d) OLR
Spring
Autumn
Winter
Annual
June
July
August
Summer

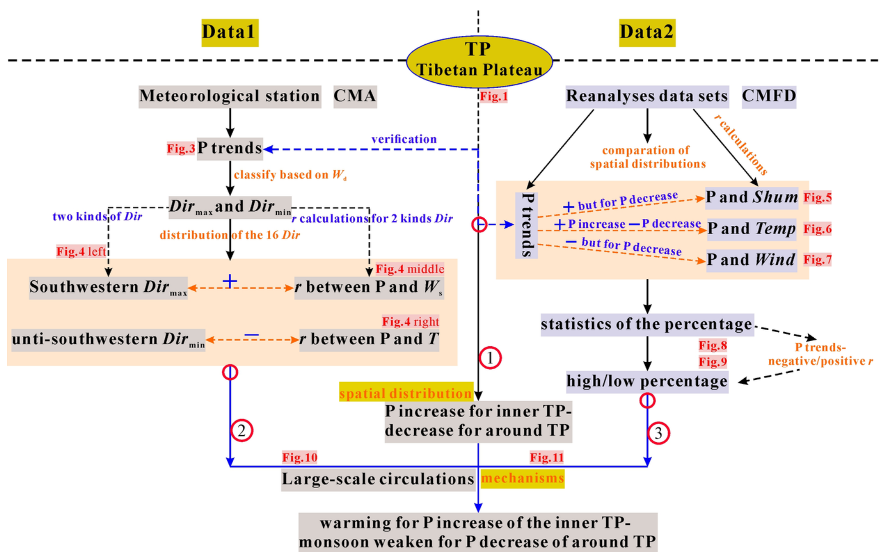
Data1
Data2
TP
Tibetan Plateau
Fig.1
Meteorological station
CMA
Reanalyses data sets
CMFD
Fig.3
P trends
verification
classify based on W_s
comparation of spatial distributions
r calculations
Dir_{max} and Dir_{min}
two kinds of Dir
r calculations for 2 kinds Dir
distribution of the 16 Dir
Fig.4 left
Fig.4 middle
Southwestern Dir_{max}
r between P and W_s
Fig.4 right
unti-southwestern Dir_{min}
r between P and T
P trends
+ but for P decrease
P and Shum
Fig.5
+ P increase − P decrease
P and Temp
Fig.6
− but for P decrease
P and Wind
Fig.7
statistics of the percentage
Fig.8
Fig.9
P trends-negative/positive r
high/low percentage
spatial distribution
P increase for inner TP-
decrease for around TP
Fig.10
Fig.11
Large-scale circulations
mechanisms
warming for P increase of the inner TP-
monsoon weaken for P decrease of around TP

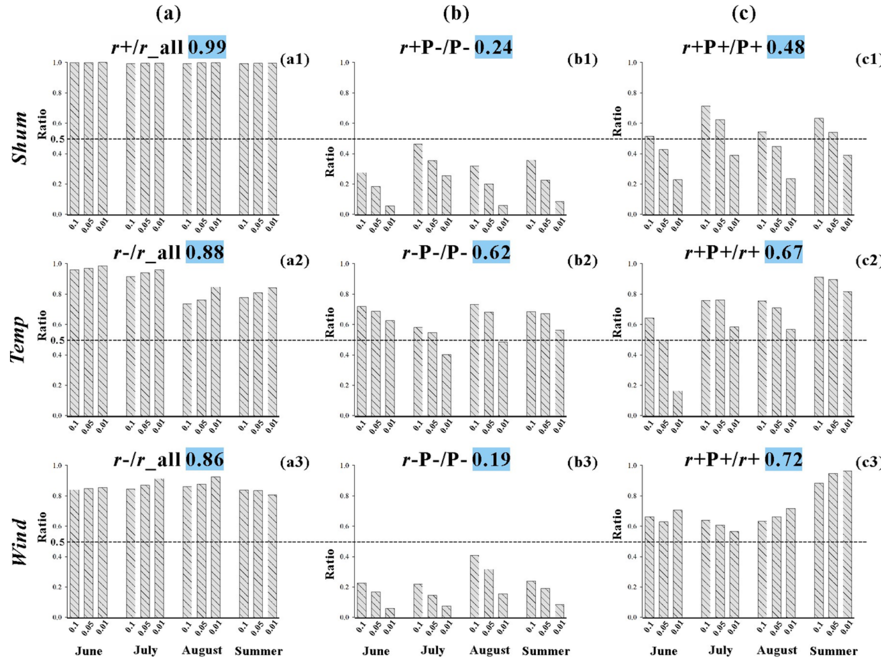
(a)
(b)
(c)
r+/r_all 0.99
(a1)
r+P-/P- 0.24
(b1)
r+P+/P+ 0.48
(c1)
r-/r_all 0.88
(a2)
r-P-/P- 0.62
(b2)
r+P+/r+ 0.67
(c2)
r-/r_all 0.86
(a3)
r-P-/P- 0.19
(b3)
r+P+/r+ 0.72
(c3)
Shum
Temp
Wind
Ratio
June
July
August
Summer

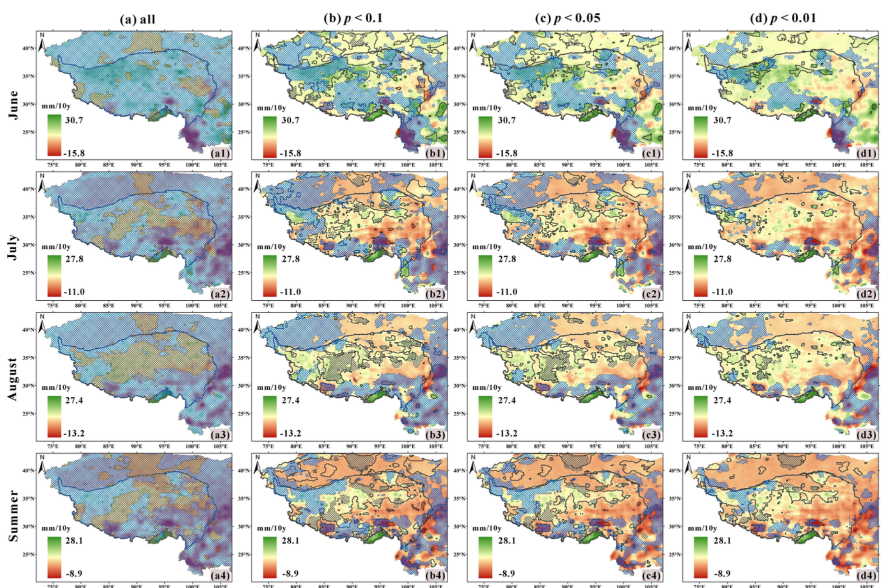
(a) all
(b) p < 0.1
(c) p < 0.05
(d) p < 0.01
June
July
August
Summer
mm/10y
30.7
-15.8
27.8
-11.0
27.4
-13.2
28.1
-8.9

Spatial patterns and possible mechanisms of precipitation changes in recent decades over the Tibetan Plateau in the context of intense warming and weakening winds

Xiaoyu Guo[1,2,*], Lide Tian[3]

[1] ECMI Team, State Key Laboratory of Tibetan Plateau Earth System Science (LATPES), Institute of Tibetan Plateau Research, Chinese Academy of Sciences, Beijing 100101, China

[2] Motuo Observation & Research Center for Earth Landscape and Earth Systems, Chinese Academy of Sciences, Beijing 100101, China

[3] Institute of International Rivers and Eco-security, Yunnan University, Kunming 650500, China

Corresponding Author: Xiaoyu Guo

Email: xiaoyuguo@itpcas.ac.cn

Address: Institute of Tibetan Plateau Research, Chinese Academy of Sciences

Lincui Road, Chaoyang District, Beijing, China, 100101

Phone: +86-13641260104；Fax: +86-10-84097079

Abstract:

The Tibetan Plateau (TP) significantly affects its surroundings and the global climate through thermal and dynamic processes. Precipitation is a key driver of hydrological, meteorological, and ecological processes. In general, the precipitation over the TP displays a wetting trend over the past half century, with large spatial heterogeneity. However, the causes of such spatially variable trends in TP precipitation and the driving forces have not been well quantified. Here we investigate the spatial variations in precipitation trends and their possible mechanisms, using ground-based observations from 132 CMA (China Meteorological Administration) stations (1970–2016) and CMFD (China Meteorological Forcing Dataset) reanalysis data (1980–2016) over the TP. The major findings are: (1) Pronounced spatial patterns of precipitation changes (increasing on the inner TP and decreasing for regions around the TP) are observed in both CMA and CMFD data. (2) Maximum precipitation decreases generally occurred in stations that experienced a southwesterly daily maximum wind speed (W_s). (3) Positive correlations between mean precipitation amount and corresponding temperature (or W_s) are obtained in directions of maximum precipitation increase (decrease), which are further verified by the qualitative and quantitative analysis of the CMFD dataset. Therefore, we suggest that intensified local recycling in a warming and hydrologically unbalanced environment has led to precipitation increases on the central TP, whereas precipitation decreases in areas bordering the TP may be the result of a weakening Indian monsoon.

Keywords: spatial patterns of precipitation changes; mechanisms; Indian monsoon; warming; Tibetan Plateau

1 Introduction

Global climate change has received considerable scientific attention in recent decades due to its pronounced impact on the world’s water and carbon cycles

(Rangwala et al., 2009; Jung *et al*., 2010), ecosystems (Knapp *et al*., 2008; Beaugrand, 2009; Guénette *et al*., 2014), and soil–plant–atmosphere interactions (Barreiro and Diaz, 2011). A marked warming of approximately 0.74 °C has been identified over the past 100 years (Mackay, 2008; Pepin and Lundquist, 2008), while greater warming rates (1–2 °C in the last century) have been reported for high-mountain regions than for lower altitude regions (Beniston *et al*., 1997; Diaz and Bradley, 1997; Qin *et al*., 2009). This suggests that hydrological cycles over high-mountain regions are more vulnerable to climate change. As the world's highest (>4,000 m above sea level (asl)) and China's largest (>2.5 million km^2) plateau (Zheng *et al*., 2000), the Tibetan Plateau (TP) has, as a whole, experienced increases in surface air temperatures over recent decades (Liu *et al*., 2009; Pepin *et al*., 2015), increased solar dimming (Shi and Liang, 2013), an increasingly moist environment (Zhang W *et al*., 2017), decreases in potential evaporation (Zhang *et al*., 2009; Wang *et al*., 2014), and weakening winds (McVicar *et al*., 2012; Lin *et al*., 2013; Guo *et al*., 2017a). Atmospheric and terrestrial thermal processes over the TP may affect Asian monsoonal rainfall (Ren *et al*., 2006), weaken thermal forcing (Ma *et al*., 2008), and exert a marked impact on both the regional climate and global atmospheric circulations (Wu *et al*., 1997; Wu and Zhang, 1998; Xu *et al*., 2008) *via* the coupling and interaction with atmospherically and hydrospherically induced climate change in the Arctic and Antarctica. Aside from the polar regions, the TP is the world's largest reservoir of solid water (in the form of glaciers, snow cover and permafrost) and the source of several large rivers (*e.g*., the Yellow, Yangtze, and Mekong rivers). As such, it is acknowledged as the "Asian Water Tower" region, supplying water to ~20% of the world's population (Immerzeel *et al*., 2010). Climate change, and especially the warming over the TP, has modified the hydrological cycle, leading to enhanced glacier retreat (Yao *et al*., 2012; Mölg *et al.*, 2014), lake expansion (Lei *et al*., 2013; Zhang G *et al*., 2013), greening (Shen *et al*., 2011; Zhang W *et al*., 2017), changes to snow cover (Wang *et al*., 2019) and groundwater storage (Zhang G *et al*., 2017), permafrost degradation (Guo *et al*., 2013; Cuo *et al*., 2015), and greater runoff yields (Yang *et al*., 2014; Su *et al*., 2016). An intensified hydrological cycle has led to dramatic regional changes, characterized by the spatial instability in water resources over the TP, which in turn has affected ecosystems (*e.g.*, increased species loss; Klein *et al*., 2004). Clearly, the subsequent socioeconomic consequences may also be considerable (Pritchard, 2019).

Precipitation is a key primary component of the global water resource and as such exerts a profound impact on the spatial distribution of other water resources and their possible variabilities (Yang *et al*., 2011; Kuang *et al*., 2016; Hrudya *et al.*, 2020). A thorough understanding of the trends and spatial patterns of precipitation changes over the TP and their possible mechanisms, set against the background of global climate change, should allow further insight into the instability shown by hydrological cycles in the Asian Water Tower region. Precipitation changes over the TP are more complicated than in other regions due to the plateau’s complex precipitation inputs from multiple moisture sources (Tian *et al*., 2001), variable transport pathways (Curio *et al*., 2013; Pan *et al*., 2019), and the frequent tectonic uplift of the region’s huge and varied topography (Qi *et al*., 2016). Therefore, these changes in precipitation have been studied for some time (Singh and Nakamura, 2009; Rajagopalan and Molnar, 2013; Gao *et al*., 2014; Li *et al.*, 2017; Zhang C *et al*., 2019; Sun *et al.*, 2021). Large-scale atmospheric circulation features such as the North Atlantic Oscillation, the Arctic Oscillation, the Indian monsoon, the westerlies, and the East Asian monsoon, as well as smaller-scale circulation arising from the intensity of local hydrological cycles, are all possible controls of spatially varying precipitation changes over the TP (Cuo *et al*., 2013; Liu *et al*., 2016; Zhang C *et al*., 2017). The effects of precipitation changes on the TP's hydrological regimes have also been investigated (Yang *et al*., 2014; Meng et al., 2019). For example, a weakening Indian monsoon has led to decreases in precipitation, thereby accelerating glacier retreat on the southeastern TP, while, conversely, significant glacier advance on the northwestern TP have been attributed to the enhanced westerlies and consequent increases in precipitation (Yao *et al*., 2012). Increased glacier mass loss and water surpluses arising from increased precipitation (Yang *et al*., 2014) are considered the most likely causes of river discharge changes on the central TP, further affecting the water budget on both local and regional scales. Although much uncertainty remains because of the sparsity of ground observations over the TP, an overall increasing trend in precipitation has nonetheless been reported (You *et al*., 2008; Yao *et al*., 2012). However, set against a general background of global warming, the spatial patterns of precipitation changes over the TP, and the possible mechanisms, merit further investigation.

To achieve this, we present herein an analysis of precipitation changes over the TP. Two sets of data were used, the ground-based observations from 132 CMA (China Meteorological Administration) stations, and CMFD reanalysis datasets (China Meteorological Forcing Dataset). For the 132 CMA stations, we analyzed the daily precipitation values, air temperatures, daily maximum wind speeds (W_s) and W_s directions over the TP during the period 1970–2016. Reanalysis data from the CMFD were used to verify the results obtained from the CMA observations. Precipitation trends and the precipitation correlations with *Shum* (specific humidity), *Temp* (temperature) and *Wind* (wind speeds) were calculated. We list the items used in this analysis in **Table 1**. This study aims to: (1) explore the spatial patterns of recent precipitation changes over the TP; and (2) reveal the possible mechanisms driving these patterns, given regional intense warming and wind weakening. We hope that our research results will improve the understanding of hydrological cycles, and further aid studies of the interactions between the land surface and the atmosphere over the TP and its surrounding regions.

2 Materials and methods

2.1 Study area

Fig. 1

Our study region lies mainly within the rectangle 20–43°N, 78–107°E, and encompasses the five western Chinese provinces, including all of Qinghai province and Tibet, and parts of Gansu, Sichuan, and Yunnan provinces (**Fig. 1**). Digital elevation models (DEM) issued by the Shuttle Radar Topography Mission (https://gisgeography.com/srtm-shuttle-radar-topography-mission/) were used to describe the general topography (asl) of the study area, which generally decreases from the northwest to the southeast. The climate over the TP is complex (Yao *et al*., 2013), due to the interaction between, and mixing of, various moisture transport pathways, including the westerlies with dry air masses (especially in the northern and western parts of the study area) (Guo *et al*., 2017; Zhang T *et al*., 2019), and the Indian monsoon with humid air masses (especially in the southern part of the study area) (Feng *et al*., 2012; Zhang Y *et al*., 2019), as well as the actions of locally recycled moisture (influencing most parts of the TP) (Curio *et al*., 2015).

2.2 Datasets

2.2.1 Ground-based measurements

The meteorological station measurements were taken from the records of the CMA (http://data.cma.cn/). The CMA dataset was quality controlled before being made publicly available. The 132 CMA stations sited across and around the TP provide records of daily precipitation amounts (mm), 2-m above ground level (agl) temperatures (daily maximum air temperature, T_{max}; daily minimum air temperature, T_{min}; daily mean air temperature, T_{mean}), 10-m agl daily maximum wind speeds (W_s), and 10-m agl directions of daily maximum wind speeds (W_d). These records cover the 47-year period 1970–2016. We removed stations from the Sichuan Basin because of the possible effects of the basin's microclimate on precipitation variability. The distribution of the 132 stations is spatially inhomogeneous (*i.e.*, dense concentrations at low altitudes and quite low concentrations at high altitudes, very few stations at west of 90°E), whilst the stations are generally equally spread in each altitudinal band from <1,000 m to ~5,000 m asl (**Fig. 1**, lower left corner).

2.2.2 Reanalysis dataset

The CMFD reanalysis dataset (from the National Tibetan Plateau Data Center: http://data.tpdc.ac.cn) was used to verify the results from the ground-based measurements. The CMFD reanalysis is generated through the fusion of remote sensing products, reanalysis datasets, and in-situ station data (Yang *et al.*, 2010; He *et al.*, 2020). Validated against ground-based measurements, the CMFD data were found to be of superior quality to the GLDAS (Global Land Data Assimilation System) dataset (He *et al.*, 2020). The CMFD is widely used in land surface process studies in China. Its spatial and temporal resolutions reach 0.1° and 3 hours, respectively. The CMFD dataset includes seven elements (2-m *Temp*, surface pressure, and *Shum*, 10-m *Wind*, downward shortwave radiation, downward longwave radiation, and precipitation rate), and is available for 1979–2018. In this study, we used records of precipitation, *Temp*, *Shum*, and *Wind* for 1980–2016. For consistency with the spatial distribution of 132 stations from the CMA, we used CMFD data within the rectangle 20–43°N, 78–107°E. For quantitative calculations of cell numbers (**Fig. 9**), the area covered by the CMFD was restricted as shown in **Fig. 8**; it includes the five western Chinese provinces and the TP within the rectangle 20–43°N, 78–107°E, but with grid cells in the Sichuan Basin removed.

The large-scale circulation patterns over the TP are shown in terms of the wind vector field and specific humidity at 500 hPa, together with the outgoing longwave radiation (OLR) in **Fig. 10**. The wind and humidity data are from NCAR (National Center for Atmospheric Research) reanalysis datasets (https://psl.noaa.gov/data/gridded/reanalysis/), at a resolution of 2.5° × 2.5° and averaged over 1981–2010. Values of OLR are another proxy for large-scale circulation over the TP. The OLR is negatively correlated with the intensity of convective activity during convective processes, whereas it is positively correlated with temperatures in winter seasons without convection (Gruber and Winston, 1978; Wang and Xu, 1997). Therefore, OLR has been used to illustrate cloudiness and rainfall in deep convection in the tropics (Risi *et al.*, 2008a, b). In this analysis, we use OLR values at a resolution of 2.5° × 2.5° from NOAA satellites (https://psl.noaa.gov/data/gridded/data.interp_OLR.html) averaged over 1981–2010. We show the seasonal and annual circulation patterns over the TP together with those in summer months (June, July, August) (**Fig. 10**).

2.3 Methods

The ISM is more intensive compared with the winter monsoon.

For this study, the four seasons are defined as follows: spring (March–May), summer (June–August), autumn (September–November), and winter (December–February). Specific details about the study periods and exact range of the study area for the two datasets (the CMA and CMFD) are given below. When detecting the spatial distribution and possible mechanisms of precipitation trends over the TP from the 132 CMA observations, precipitation trends and the correlations of precipitation with temperature or W_s were calculated for the four seasons and annually for various sub-periods during 1970–2016. Regions over the TP experienced significant air warming and wind weakening (Guo *et al.*, 2017a). We mentioned that Indian monsoon are the main supplies of moisture origins and played a key role in precipitation patterns in the TP (especially the southern TP) both in summer and in winter months (Nair *et al.*, 2018; Kuttippurath *et al.*, 2021). Large-scale circulation patterns in the summer months exhibit significant spatial variability (*e.g.*, local circulation or the westerlies for the northern TP, and the Indian summer monsoon and humid air masses in the south) (Yao *et al.*, 2013). This is also seen in the circulation patterns presented in **Fig. 10**. Therefore, precipitation patterns in summer months were specifically selected during the verification processes using the CMFD reanalysis. The spatial patterns of precipitation change and the correlations with possible controlling factors are captured well in summer, and the linkage to global warming and wind weakening over the TP is further investigated. For ground-based observations from the CMA, 132 stations during 1970–2016 were used. The CMFD dataset encompass periods 1979–2018, and we used data during 1980–2016 for consistency with the CMA data as much as possible. The comparatively large altitudinal range of ~4,500 m (from the Yuanjiang Station in Yunnan Province at 397 m asl to the Anduo Station in Tibet at 4,801 m asl), the generally equally spread numbers of stations for each altitudinal band (lower left in **Fig. 1**), the complex climatic conditions, various sources of moisture and vast topographical range, as well as intense climate changes set against a background of global and regional warming, make our study region an ideal area for the observation of the spatial distribution of precipitation changes over recent decades and investigation of the possible mechanisms. Datasets from both ground-based measurements (CMA) and reanalysis (CMFD) ensure the high reliability of results.

Fig. 2

Figure 2 sets out the general framework in this study. Two sets of data (*i.e.*, the 132 CMA stations and the CMFD reanalysis) were used to reveal and verify the spatial patterns and possible mechanisms of precipitation changes in recent decades over the TP. For the CMA datasets, we followed the steps outlined below to describe the precipitation patterns over the TP. In **Table 2**, the general steps to achieve the spatially precipitation patterns for datasets of CMA and CMFD are both list and compared, with corresponding Figures also provided. (1) *Trend analysis of precipitation*. We calculated the linear trends of precipitation for the four seasons and annually for eight sub-periods between 1970 and 2016 (*i.e.*, 1970–2016, 1980–2016, 1990–2016, 2000–2016, 1970–1979, 1980–1989, 1990–1999, and 2000–2009). Results are plotted in **Fig. 3** (summer) and **Figs S1**–**S4** (spring, autumn, winter, and annually). To clarify the possible causes of spatial variability in the rates of precipitation change from the aspect of water and energy availability, which may differ with height due to the varying altitudes, linear correlations of precipitation trends with the corresponding altitudes were then computed (**Table 2**). (2) *Classification of precipitation trends based on W_d of the 132 stations*. We classified the precipitation trends in Step (1) into 16 groups, based on the W_d values of the 132 CMA stations. For each of the 16 groups in each sub-period during 1970–2016, we then calculated the average rates of change. We did this for all of the stations and for those with precipitation trends significant at $p < 0.1$. Then the maximum and minimum cluster-averaged values and the corresponding W_d (Dir_{max} and Dir_{min}) were selected (panel (a) in **Fig. 4**). (3) *Correlations of precipitation amount and W_s or temperature*. For the *Dir*s (Dir_{max} and Dir_{min}) selected in Step (2) (panel (a) in **Fig. 4**), we analyzed the linear correlations (r) between precipitation amount and corresponding temperatures (T_{max}, T_{min}, and T_{mean}) or W_s (panels (b) and (c) in **Fig. 4**). All elements for the regressions were averaged for each of the 16 groups. (4) *Comparative analysis for Dirs*. Statistics on Dir_{max} and Dir_{min} (panel (a) in **Fig. 4**) were plotted for comparison with those obtained using the correlations (panels (b) and (c) in **Fig. 4**). We then identified whether there are consistent relationships between Dir_{max} and Dir_{min}, and those *Dir*s for positive or negative r values. (5) *Possible mechanisms for precipitation trends in TP*. From the spatial patterns of precipitation trends (**Fig. 3**, **Figs S1**–**S4**), and the clustering results in **Fig. 4**, and combining these with the large-scale circulation over the TP (**Fig. 10**), we tried to identify possible mechanisms for the spatial patterns of precipitation trends. In this step, it is essential to understand the background of the large-scale circulation and climate change (*e.g.*, warming, monsoon weakening) in recent decades. Note that summer precipitation appears to be the most representative (compared with other seasons), because of its higher contribution to annual precipitation and the comparatively complex climatic conditions induced by the combined influence of various moisture sources. Spatial patterns of changes in precipitation during the summer months are therefore a particular focus of our analysis and are shown in the main paper as **Fig. 3**, while those for other seasons and annually are presented in the appendix (**Figs S1**–**S4**).

The CMFD reanalysis was used to verify the results from the CMA observations.

The detailed steps were as follows. (1) *Analysis of precipitation trends*. Firstly, we calculated the CMFD precipitation trends for each month in summer and the whole summer between 1980 and 2016. All the rates of change of precipitation and those significant at various p values ($p < 0.1$, $p < 0.05$, $p < 0.01$) are presented (**Figs 5–7**). (2) *Correlations between precipitation and Shum/Temp/Wind*. The linear correlation coefficients between precipitation and *Shum*/*Temp*/*Wind* from the CMFD reanalysis were calculated for periods 1980–2016. All the r values and those significant at $p < 0.1$, $p < 0.05$, $p < 0.01$ are shown, with the precipitation trends obtained in Step (1) as the background (**Figs 5–7**). (3) *Comparisons of the spatial distributions in Steps (1) and (2)*. We plot the precipitation trends (Step (1)) and r values (Step (2)) in individual figures (**Fig. 5**, *Shum*; **Fig. 6**, *Temp*; **Fig. 7**, *Wind*). Positive or negative precipitation trends and r values are identified by different symbols. In this step, we identify relations between the spatial distributions of precipitation trends and the negative or positive r values that are obtained from correlations of precipitation and *Shum*/*Temp*/*Wind*. (4) *Quantitative ratio calculations*. Finally, the proportions of cells with precipitation increases or decreases and positive or negative r values defined in terms of correlation with humidity, temperature wind were calculated. The ratios in summer months, and for those precipitation trends or r values significant at $p < 0.1$, $p < 0.05$, $p < 0.01$ are calculated (**Fig. 9**). Comparatively higher or lower percentages for precipitation increases or decreases and sets of cells defined by positive or negative correlations between precipitation and Shum/Temp/Wind_suggest high reliability of the results from the 132 CMA stations.

Linear regression is adopted in this analysis to calculate precipitation trends, the linear correlations between precipitation trends and corresponding altitudes asl, and the linear correlations between precipitation amounts and W_s/temperatures (T_{max}, T_{min}, and T_{mean}) or *Shum*/*Temp*/*Wind*, as shown below:

$$y = a\,x + b \qquad (1)$$

For trend analysis, y denotes the precipitation amount, and x represents the time (in years); for linear correlation analysis, y represents the precipitation trends or precipitation amount, and x denotes the corresponding altitude, W_s values, temperature (T_{max}, T_{min}, and T_{mean}) or *Shum*/*Temp*/*Wind*. a is the slope (changing rates of precipitation, variability of precipitation trends with altitude, precipitation changes dependent on possible controlling factors as W_s, temperature or *Shum*/*Temp*/*Wind*), and b is the intercept.

We determined the regression parameters a and b using least squares fitting method. The statistical significance of the changes in rates (precipitation amount *versus* time, precipitation trends *versus* altitude, precipitation amount *versus* the controlling factors W_s, temperature or *Shum*/*Temp*/*Wind*) were evaluated using the Student's t-test as follows:

$$t = r\,[(n - 2) / (1 - r^2)]^{1/2} \qquad (2)$$

where n represents the total number of samples analyzed (the number of years, the number of CMA stations or the number of grid cells) and r represents the correlation coefficients between x and y in Equation (1).

The general procedures used to investigate spatial patterns of precipitation change in recent decades and the mechanisms responsible over the TP are as follows. (1) With the 132 CMA stations, we calculated the precipitation trends (**Fig. 3**, **Figs S1–S4**), clustered them into 16 groups based on W_d of the 132 stations, and identified the Dir_{max}, Dir_{min} for each sub-period during 1970–2016 (panel (a) in **Fig. 4**). (2) For groups of Dir_{max} and Dir_{min}, correlations between clustered-averaged precipitation amount and corresponding W_s or temperature (T_{max}, T_{min}, T_{mean}) were analyzed (panels

(b) and (c) in **Fig. 4**). We then compared the *Dir*s of $Dir_{\max}$ and $Dir_{\min}$ with those obtained using the correlations (**Fig. 4**). (3) Precipitation trends were recalculated using the CMFD reanalysis for summer months (and the whole summer) over 1980–2016 (**Figs 5–7**). The results were compared with those from Step (1). (4) With the CMFD, we regressed precipitation amount against *Shum*/*Temp*/*Wind*. The r values at various confidence levels ($p < 0.1$, $p < 0.05$, $p < 0.01$) were plotted, with precipitation trends as the background (**Figs 5–7**). (5) Quantitative statistics of precipitation trends and positive/negative r values (Step (4) over the area defined in **Fig. 8**) are presented in **Fig. 9**. (6) We show the possible mechanisms for the spatial patterns of precipitation trends, combining the results from the CMA and the CMFD, under the background conditions of warming and weakening wind over the TP (**Fig. 11**).

3 Results

3.1 Spatial patterns of precipitation trends from CMA observations

Fig. 3

Figs S1–S4

Figure 3 and **Figs S1–S4** show the spatial distribution of precipitation trends across the four seasons and annually during each period within the 1970–2016 timeframe. In contrast to the consistency shown in wind speed decreases (Yang *et al.*, 2014; Guo *et al.*, 2017a) and warming (Qin *et al.*, 2009; Guo *et al.*, 2016) observed over the TP in previous studies, we detected no homogeneous increasing or decreasing trends in precipitation. Summer precipitation experienced the most severe changes (increasing or decreasing; **Fig. 3**), while the smallest amplitude in trends was detected in winter (**Fig. S3**). To test the sensitivity of these precipitation trends, similar analyses of various periods during the 1970–2016 timeframe were conducted;

viz. 1980–2016, 1990–2016, 2000–2016, 1970–1979, 1980–1989, 1990–1999, and 2000–2009. From the increase in the number of stations with stronger precipitation trends and the increasing numbers of stations significant at $p < 0.1$ in the left-hand panels of **Fig. 3** and **Figs S1**–**S4**, it is reasonable to conclude that changing rates in precipitation (both increases and decreases) have generally intensified over the past 47 years for all seasons and annually. No uniform temporal characteristics of precipitation trends were found in any decade (panel (b) in **Fig. 3** and **Figs S1**–**S4**). Spatially distinct patterns in precipitation trends are seen except for 1970–1979, and for 1980–1989 during some seasons, and can be generally categorized as increases on the central TP and decreases in regions around the TP.

3.2 Precipitation trends with altitude

Table 2

Altitudes in the hinterland of the TP are higher, but are lower in the peripheral regions of our study area, thereby determining the vertical and/or altitudinal distributions of the water and energy budgets, and further affecting the spatial patterns of precipitation changes to some extent. Changes in precipitation rates were then regressed against altitude for each stated period within 1970–2016, with results listed in **Table 2**. We found that precipitation generally increased (decreased) at higher (lower) altitudes, and that the rates of change were enhanced with increasing (decreasing) altitude. Exceptions were found during winter and the periods 1970–1979 (autumn, insignificant at $p < 0.1$) and 1990–1999 (summer, insignificant at $p < 0.1$). Even given different starting years for the different analysis periods between 1970 and 2000 (see the four left-hand columns in **Table 2**), the dependency of precipitation changes on altitude are weakened for both all the 132 stations counted, and for the mean values of each altitudinal band. The dependency of precipitation changes on altitude is strongest for the longest period of 1970–2016.

3.3 Precipitation and temperature or W_s

Fig. 4

To reveal the effect of climate change on the spatial changes of precipitation over the TP, we clustered precipitation trends of the 132 stations into 16 groups, based on the W_d values, which are recorded in 16 directions in CMA and may varied during different seasons and in various study periods. Rates of precipitation change and meteorological variables (*e.g.*, precipitation amount, T_{max}, T_{min}, and T_{mean}, W_s) were averaged for each of the 16 groups. All 132 stations, and only those with precipitation trends significant at $p < 0.1$, were considered. The overall W_d of maximum and minimum precipitation trends (Dir_{max}, Dir_{min}) were selected for each study period and plotted in panel (a) of **Fig. 4**; the linear correlations between precipitation amounts and corresponding temperature (T_{max}, T_{min}, and T_{mean}) and W_s values for the selected directions (Dir_{max}, Dir_{min}) are shown in panels (b) and (c) of **Fig. 4**. Note that correlation coefficients of < 0.1 (absolute value) were not counted.

In panel (a) of **Fig. 4**, maximum precipitation decreases (Dir_{min}, red dots) are mainly distributed in a southwesterly direction in clusters 9−12, this being especially true for spring, summer, autumn, and annual values, indicating that meteorological stations dominated by the southwesterly W_s experienced the highest decreases in precipitation over the TP, except during the winter period. The greatest increases in precipitation corresponding to Dir_{max} (blue dots) are spread across various directions in different seasons. The directions are inconsistent: 5−8 and 13 in spring, 5 and 7−8 in the summer, 6−13 in the autumn, and 6−8 and 10−13 annually. Few Dir_{max} were observed to extend in southwesterly *Dir*s, especially during the spring, summer, autumn, and annually. We note that *Dir*s of precipitation trend extremes (both maxima and minima) during the winter (clusters 7–14) showed no consistent dependence on direction. Correlation coefficients in panels (b) and (c) in **Fig. 4** should be compared with the directions (Dir_{max}, Dir_{min}) shown in panel (a). Both positive (red symbols) and negative (blue symbols) correlations were observed. The *Dir*s of the positive correlations with temperatures (panel (b) in **Fig. 4**, red) were generally the same as the Dir_{max} (panel (a) in **Fig. 4**, blue; especially in spring, summer, and annually), and positive correlations with W_s (panel (c) in **Fig. 4**, red) were mainly spread across ranges similar to the Dir_{min} (panel (a) in **Fig. 4**, red; especially in summer, autumn, and annually). As shown in **Fig. 4**, and excluding any winter results, we uniformly found maximum precipitation decreases for stations with southwesterly W_d (panel (a) in **Fig. 4**), relatively consistent *Dir*s for positive correlations of precipitation with temperature (panel (b) in **Fig. 4**), and for Dir_{max} (panel (a) in **Fig. 4**), and relatively consistent *Dir*s for positive correlations with W_s (panel (c) in **Fig. 4**), and for Dir_{min} (panel (a) in **Fig. 4**), discounting some minor disturbance.

3.4 Spatial patterns of precipitation trends from CMFD reanalysis

Fig. 5

The CMFD reanalysis was also used to detect the spatial distribution and possible mechanisms of recent precipitation changes over the TP. In addition, the study of the CMFD reanalysis may verify results from the CMA observations. For spatial patterns of precipitation trends, the CMFD data covered the same rectangle (20–43°N, 78–107°E) as the 132 CMA stations. We show the summer precipitation trends during periods 1980−2016 as colored shading in **Figs 5**–**7**, for all the grid cells (panel (a) in **Fig. 5**) and those with precipitation trends significant at $p < 0.1$ (panel (b) in **Fig. 5**), $p < 0.05$ (panel (c) in **Fig. 5**), and $p < 0.01$ (panel (d) in **Fig. 5**). The borders for precipitation trends at each confidence level ($p < 0.1$, $p < 0.05$, and $p < 0.01$) are marked as black solid lines, with the precipitation trends as the background. Since the precipitation trends used as background in **Figs 5–7** are exactly the same, we therefore take those in **Fig. 5** as representative.

We detect increases in summer precipitation on the main body of the TP (green in **Fig. 5**), especially on the northern and central TP. For regions of the southern TP or around the TP, precipitation was decreasing (red in **Fig. 5**). With the confidence level changing from $p < 0.1$ to $p < 0.05$, and then $p < 0.01$, the most severe and significant precipitation increases are found on the northern border of the TP (bold black lines in **Fig. 5**), while grid cells with significant precipitation decreases are mainly located on the southern and eastern border of the TP. This is true for all the summer months. For monthly comparisons from June to August, precipitation in June experienced more severe increases on the central TP, with both higher rates of change of precipitation and more cells with precipitation increases (**Fig. 5**(d1)). There are more grid cells with negative precipitation trends in July (**Fig. 5**(d2)) and August (**Fig. 5**(d3)) than in June. In other words, we generally see widespread deep green (precipitation increases) in June (**Fig. 5**(d1)), whereas more grid cells with red backgrounds (precipitation decreases) can be seen in July and August (**Fig. 5**(d2) and (d3)).

3.5 Precipitation and ***Shum*/*Temp*/*Wind***

Figs 5−7

Shum, *Temp*, and *Wind* are important controls of water and energy redistribution. With the CMFD reanalysis, the linear correlations between precipitation amount and

Shum/*Temp*/*Wind* during summer and each summer month in 1980−2016 were analyzed. To highlight the spatial distribution of precipitation trends and positive/negative *r* values obtained for correlations between precipitation and *Shum*/*Temp*/*Wind*, the correlations are drawn on a background showing the summer precipitation trends (**Figs 5**−**7**). The results may help identify the controls of spatial changes in precipitation over the TP. The colored crosses in **Figs 5−7** indicate positive (black) and negative (blue) correlations obtained between precipitation with *Shum* (**Fig. 5**), *Temp* (**Fig. 6**), and *Wind* (**Fig. 7**). Negative or positive correlations for all the grid cells (panel (a) in **Figs 5**−**7**), and those significant at $p < 0.1$ (panel (b) in **Figs 5**−**7**), $p < 0.05$ (panel (c) in **Figs 5**−**7**), and $p < 0.01$ (panel (d) in **Figs 5**−**7**) are all shown. For each panel in **Figs 5**−**7**, the precipitation trends shown as the background have the same confidence level as the correlations between precipitation and *Shum*/*Temp*/*Wind*.

Fig. 5

Correlations between precipitation and *Shum* presented in **Fig. 5** are mainly positive. The spatial distribution of positive *r* values spreads across the central TP, where there are significant precipitation increases. Cells with positive *r* values (black crosses in **Fig. 5**) do not overlap cells with precipitation decreases (red background in **Fig. 5**). This is especially true for calculations significant at the $p < 0.1$, $p < 0.05$, and $p < 0.01$ confidence levels, in which significant precipitation decreases are indicated by the black boundary with the red background in **Fig. 5**. In other words, for relations between precipitation and *Shum*, we detected closer positive relations in regions with significant summer precipitation increases, whereas no clear relations were found for regions of precipitation decreases, with the confidence level changing from $p < 0.1$ to $p < 0.05$ and $p < 0.01$.

Fig. 6

In **Fig. 6**, more cells with negative correlations (blue crosses) between precipitation and *Temp* are evident. With confidence level changing from $p < 0.1$, to $p < 0.05$, to $p < 0.01$, very few positive r values were found, and they were mainly scattered among cells with significant precipitation increases on the central TP. Negative r values were mainly spread across regions around the margin of the TP. We found that cells with significant precipitation decreases (black border with red background in **Fig. 6**) generally have significant negative r correlations (black crosses in **Fig. 6**). This is true for $p < 0.1$, $p < 0.05$, and $p < 0.01$. In conclusion, close relations were found between precipitation and *Temp* on the central and northern TP, in the form of positive correlations for cells with significant summer precipitation increases. Significantly negative r values detected in regions around the margin of TP agreed with results from the 132 CMA stations (panel (b) in **Fig. 4**).

Fig. 7

The correlations of precipitation amount and *Wind* during summer and each summer month in 1980–2016 are shown in **Fig. 7**. Grid cells in the rectangle 20–43°N, 78–107°E in our study area generally showed negative correlations. Positive r values are found both in regions of the central TP and around the margins of the TP (panel (a) in **Fig. 7**). With p values changing from $p < 0.1$, to $p < 0.05$, and $p < 0.01$, the area with significant r values became smaller. Positive r correlations were generally spread over regions of the northern TP, within the northern border of the TP. This is especially true for $p < 0.1$ (panel (b) in **Fig. 7**), $p < 0.05$ in June (**Fig. 7**(c1)) and summer averages at $p < 0.01$ (**Fig.** 7(d4)). We note that precipitation trends in the northern border of the TP are generally positive. No spatially uniform patterns are found for negative r correlations. Note that cells with significantly negative r values (blue crosses) are generally not located in regions with significant summer precipitation decreases (black border with red background in **Fig. 7**). Significantly negative *r* values (blue crosses) are also found for cells with precipitation increases (black border with green background in **Fig. 7**). From the northwest to the southeast of our study region, the *r* values between precipitation and *Wind* change from significantly positive (northwestern region), to significantly negative (the central TP), and no correlations or insignificant *r* values (southeastern region). The spatial patterns are especially clear for $p < 0.05$ (panel (c) in **Fig. 7**) and $p < 0.01$ (panel (d) in **Fig. 7**).

Fig. 8

Fig. 9

Statistics for various ratios of positive and negative precipitation trends (P−/P+) and correlation coefficients (*r*+/*r*−) between precipitation and *Shum*/*Temp*/*Wind* are shown in **Fig. 9**. The exact area considered is shown in **Fig. 8**(e). We retain grid cells including the five western Chinese provinces (Tibet, Qinghai, Gansu, Yunnan, and Sichuan) within the TP boundary, while grid cells outside the rectangle 20–43°N, 78–107°E and in the Sichuan Basin are removed. The area covered in **Fig. 8**(e) and **Fig. 9** is consistent with the exact locations of the 132 CMA stations (**Fig. 1**). In **Fig. 9** the *x* axis shows the confidence level ($p < 0.1$, $p < 0.05$, and $p < 0.01$) for each of the summer months. Numbers with a blue background are the averaged ratios for each sub-figure. The various ratios in **Fig. 9** are labelled as follows: taking "*r*−/*r*_all" (**Fig. 9**(a2)) as an example, this is the ratio of cells with negative correlation coefficients *r* between precipitation and the quantity labelled on the left (*e.g.*, *Temp*, *Wind*) to the number of cells with all values of *r* in a certain month and at a certain confidence level. Similarly, "*r*−P−/P−" means the ratio of all cells in which the precipitation decreased that also had a negative correlation with defined climate factors (*e.g.*, *Shum*, *Temp*, and *Wind*).

For correlations of precipitation with *Shum*, the proportions of positive r values (r+/r_all) reach 99% (**Fig. 9**(a1)). The proportion of all cells with precipitation decreases that also have positive r values (r+P−/P−) is as low as 0.24 on average (**Fig. 9**(b1)). As the confidence level changes from $p < 0.1$, to $p < 0.05$, and $p < 0.01$, the former proportion decreases to values < 0.1. The proportion of cells with precipitation increases that also have positive r values (r+P+/P+) is much higher at 0.48 (**Fig. 9**(c1)). Ratios of "r+P+/P+" exceed 0.5 for $p < 0.1$ and $p < 0.05$ in July and summer.

Under the background conditions of global warming and weakening wind over the TP, we also analyze correlations of precipitation with *Temp* or *Wind* and compare the statistics (the middle and lower panels in **Fig. 9**). The negative r proportions (r−/r_all) are high for both *Temp* and *Wind*, reaching 0.88 (**Fig. 9**(a2)) and 0.86 (**Fig. 9**(b3)), respectively. The proportions are as high as 0.62 for cells with precipitation decreases that also have negative correlations with *Temp* (r−P−/P−) (**Fig. 9**(b2)); higher values of r−P−/P− (> 0.7) in **Fig. 9**(b2) occurred at the $p < 0.1$ confidence level. Much lower values of 0.19 (r−P−/P−) are found for the correlation against *Wind* (**Fig. 9**(b3)), with minimum values of < 0.1 for $p < 0.01$. Positive r correlations between precipitation and *Temp* are generally strongly associated with cells with precipitation increases, as illustrated by the high percentages of 0.67 (r+P+/r+) in **Fig. 9** (c2). In **Fig. 9** (c3), the grid cells that have positive r with *Wind* have a high proportion of 0.72 for cells with precipitation increases (r+P+/r+). This is especially true for cells significant at $p < 0.01$ (**Fig. 9**(c3)). We note that both the *Temp* and *Wind* play important positive roles for precipitation changes in regions with precipitation increases (**Fig. 9**(c2), (c3)).

4 Discussion

4.1 Spatial patterns of precipitation change

Spatial patterns of precipitation change taken from both the CMA observations (**Fig. 3**, **Figs S1–S4**) and the CMFD reanalysis (**Figs 5–7**) in this study agree with the results presented in previous research (Yin *et al*., 2013; Yao *et al*., 2013; Tong *et al*., 2014; Deng *et al*., 2017; Zhang C *et al*., 2017; Yang K, 2021). In general, precipitation for regions in the central and northern TP is increasing, whereas in regions around the margin of the TP, significant precipitation decreases have been observed in recent decades. Precipitation is one of the most important sources for the hydrological cycle and thus has a marked impact on the spatial distribution and variability of other water resources. Relatively consistent spatial patterns in changes to glacial coverage (Kang *et al*., 2010; Yao *et al*., 2012), snow cover (Chen *et al*., 2017; Wang *et al*., 2019), permafrost (Cheng *et al*., 2007; Guo *et al*., 2013), lake volume (Song *et al*., 2014; Yang *et al*., 2017), soil moisture (Yang *et al*., 2011), river runoff (Yang *et al*., 2014) and water storage (Meng *et al*., 2019) appear to correlate with changes in precipitation over recent decades observed over the TP, confirming the reliability of our results.

4.2 Physical drivers: from climate variables

A positive relation was generally found from the linear regressions of rate of change of precipitation from CMA stations against altitude (**Table 2)**. Precipitation from the CMA stations generally increased (decreased) at higher (lower) altitudes, and the rates of change were enhanced with increasing (decreasing) altitude. The altitudes of our study area showed a rough trend of “low to high” from the southeastern to northwestern TP, which further affects the vertical distribution of water and energy over the TP. The generally positive r values in **Table 2** indicate that altitude has some effect on the spatial patterns of precipitation changes over the TP, as widely reported in previous studies (Li *et al.*, 2017). Negative relations were also found in winter and in 1970–1979 (autumn, insignificant at $p < 0.1$), 1990–1999 (summer, insignificant at $p < 0.1$). In addition, in the four left-hand columns in **Table 2**, the altitude dependency of precipitation changes generally weakens as the start year of the analyzed period changes from 1970 to 2000. This is true when all 132 CMA stations (without background in **Table 2**) are considered, and also within each altitudinal band (with gray background in **Table 2**).

Over recent years, climate change over the TP has generally amplified (Guo *et al.*, 2017a), while the subsequent influence on the vertical distributions of the water and energy budgets, as represented by the altitudinal dependency of precipitation trends, has weakened in inverse proportion (**Table 2**, the four left-hand columns). The question here therefore concerns the possible mechanisms behind, and drivers of, such spatial patterns of precipitation trends over the TP. In the work of Guo *et al*. (2017a), consistently enhanced, altitude-dependent changes in both wind speed and temperatures (especially T_{min}) during the 1970–2012 period were observed, contrary to the weakening altitudinal dependency of precipitation changes propounded in this analysis. Using spatially continuous, satellite-based datasets over and around the TP, Guo *et al*. (2019) reported a reversal in "altitude-dependent warming" at higher altitudes as shown by the decreases in rates of warming in regions >4,500 m asl (consistent with patterns of nighttime cloud and snow cover). This suggests that the altitude-dependent changes in climate variables (*e.g.*, temperature, wind speed, and precipitation) based on land surface measurements may be difficult to diagnose because of the relative sparsity of observations at >5,000 m asl. Controls other than altitude must affect the spatial distribution of precipitation trends over the TP.

The spatial or vertical redistributions of water and energy budgets are intricately connected with changes in climatic variables such as temperature and wind (Guo *et al*., 2016). Given the background of global and regional air warming (Liu *et al*., 2009; Qin *et al*., 2009; Pepin *et al*., 2015) and consistent decline in wind speed (Lin *et al*., 2013; Guo *et al*., 2017a) over the TP, the roles these variables play in the spatial patterns of precipitation trends is an interesting, and relatively unexplored, theme. Moisture sources and transport pathways, the main controls of precipitation, are both closely correlated with W_d, and the effect of W_d on precipitation changes over the TP merits further exploration.

The clustering of the 16 groups in **Fig. 4** is striking. Stations affected by southwesterly maximum winds (W_d) (groups of 9–12) are mainly located in the southern TP or regions around the margin of the TP (**Fig. 1**, **Fig. 10**); these are the stations that experienced maximum precipitation decreases (**Fig. 3**, **Figs S1**–**S4**, and red dots in panel (a) of **Fig. 4**) and exhibit a positive correlation between precipitation and W_s (red symbols in panel (c) of **Fig. 4**). These results indicate that wind speed (upper-air wind and W_s) plays a profound role in the precipitation decreases in regions around the TP. For the CMA stations located in regions affected by the westerlies or the locally recycled air masses of the inner TP (**Fig. 1**, **Fig. 10**), precipitation is significantly increased (**Fig. 3**, **Figs S1**–**S4**, and blue dots in panel (a) of **Fig. 4**). We also observed similar *Dir*s of maximum precipitation increases (Dir_{max}; blue dots of panel (a) in **Fig. 4**) and positive correlations between precipitation and temperatures (red symbols of panel (b) in **Fig. 4**), which further illustrates the impact of warming on precipitation increases on the central TP (**Fig. 3**, **Figs S1**–**S4**).

The spatial distributions of correlations between precipitation and

Shum/*Temp*/*Wind* are presented in **Figs 5–7**, with precipitation trends from CMFD reanalysis as the background. The corresponding quantitative statistics are presented in **Fig. 9**. Spatially, positive r for correlations with *Shum* are mainly distributed on the central TP and do not overlap cells with significant precipitation decreases (**Fig. 5**); this is further verified by the low r+P−/P− value of 0.24 in **Fig. 9**(b1) and the much higher r+P+/P+ value of 0.48 in **Fig. 9**(c1). In **Fig. 6**, positive r correlations between precipitation and *Temp* are distributed on the central TP, with comparatively high ratio for r+P+/P+ of 0.67 (**Fig. 9**(c2)). In contrast, negative r correlations are distributed on the southern TP, with the ratio for r−P−/P− of 0.62 (**Fig. 9**(b2)). Positive correlations between precipitation and *Wind* are found for regions with both precipitation increases and decreases (**Fig. 7**), while significantly negative r values are not seen for cells with precipitation decreases, which can be verified by the low ratio for r−P−/P−, 0.19 in **Fig. 9**(b3). The corresponding spatial patterns and quantitative analysis using the CMFD reanalysis coincide with those observed from the CMA observations (panels (b) and (c) in **Fig. 4**). The high proportions of 0.72 observed in r+P+/r+ in **Fig. 9**(c3) seems unreasonable and is discussed in the following paragraph.

For the CMFD reanalysis, and for the northern TP, positive correlations were found both in **Fig. 6** (precipitation and *Temp*) and **Fig. 7** (precipitation and *Wind*). In **Fig. 5** (precipitation and *Shum*), the r values at the northwestern TP are also positive. The general positive relations between precipitation amount and *Shum* over the TP (**Fig. 5**) are reasonable and easy to understand. The higher the *Shum*, the higher the precipitable water vapor, which further determines the patterns of precipitation amount and precipitation variability. The other factors, *Temp* and *Wind*, may influence precipitation distributions and precipitation trends by either directly or indirectly affecting water and energy redistribution. The positive r values between precipitation and temperatures (panel (b) in **Fig. 4**, *T*; and **Fig. 6** *Temp*) observed in the central and northern TP are related to enhanced evaporation, *Shum* increases, and an intensified hydrological cycle. The intensified hydrological cycle may be induced by or closely connected with temperature rises, and results in precipitation increases. With the CMFD reanalysis, we detected significant positive correlations between precipitation and *Wind* for the central and the northern TP, where precipitation increased significantly (**Fig. 7**). These positive results on the inner TP from *Wind* also make sense, considering the large-scale circulation patterns over our study region. For the inner or northern TP regions, comparatively dry air masses from the westerlies or locally recycled masses are the main controls of precipitation patterns (Tian *et al.*, 2001; Yao *et al.*, 2013). Humid air associated with the Indian summer monsoon can only reach the northern TP via intensive monsoonal processes (Guo *et al.*, 2017), while the subsequent monsoonal precipitation over the northern TP is extremely limited. The W_s of CMA indicates the daily maximum wind speed and can represent winds at large-scale; *Winds* from the CMFD are the near-surface winds and more closely connected with local air masses. Therefore, for regions of the northern TP, *Wind* from the CMFD reanalysis refers to the winds of the westerlies or from the locally recycled air; W_s from the 132 CMA stations may represent winds from both the westerlies or local air and the Indian monsoon. Considering that air masses from the westerlies or local recycling are comparatively dry, changes in absolute water vapor content along with this kind of wind are negligible. Thus, the positive relations between precipitation and *Wind* for the northern TP mainly relate to accelerated water and energy exchange between the land surface and the upper atmosphere, enhanced evapotranspiration, and a further intensified hydrological cycle, bringing more water vapor into the atmosphere. In a word, higher winds accelerate air disturbance and increase the amount of water vapor in the atmosphere, resulting in precipitation increases in the northern TP regions. In panel (c) of **Fig. 4**, positive correlations between precipitation and W_s are mainly spread over the southwesterly *Dir*s, while positive correlations are also found for the western *Dir*s. For example, positive r values are observed in *Dir*s of 12 in summer (**Fig. 4**(c2)), 13 in spring (**Fig. 4**(c1)), and 14 in winter (**Fig. 4**(c4)), which may relates to the westerlies winds for northern TP regions. Results from the CMA (panels (b) and (c) in **Fig. 4**) are consistent with the positive relations observed between precipitation and *Temp*/*Wind* for the inner TP regions (**Figs 6** and **7**). The intensity of the Indian monsoon is strongest in summer, and the areas affected by the westerlies or the local air masses spread farther over the TP in seasons other than summer (**Fig. 10**). *Wind* in the northern TP is more closely related to the intensity of water and heat exchange with the land and upper atmosphere but not the intensity of humid air mass transportation, particularly outside the summer months. The positive correlations between precipitation and W_s detected in *Dir*s 14 (in winter) and 13 (in spring) rather than 12 (in summer; summer: *Dir* 12 slightly overlaps with the directions of the Indian summer monsoon; panel (c) in **Fig. 4**) are reasonable. Since the results presented in panel (c) of **Fig. 4** show only those obtained from Dir_{max} and Dir_{min} (panel (a) in **Fig. 4**), and the W_s (from CMA) differs from *Wind* (from the CMFD), the positive relations between precipitation and W_s or *Wind* may not be totally equivalent between the CMA and the CMFD datasets.

The qualitative (**Figs 3**–**4** and **Figs 5**–**7**) and quantitative (**Fig. 9**) analysis of spatial precipitation patterns from both the ground-based observations (the 132 CMA stations) and reanalysis datasets (the CMFD) have improved our understanding of precipitation changes and their possible physical drivers. Under the background of global climate change, precipitation patterns over the TP are extremely complex and affected by multiple controlling factors. Therefore, composite analysis of such spatial patterns of precipitation should be performed for various controlling factors in combination with the background of warming and wind weakening over the TP. We discuss this further in the following section.

4.3 Possible mechanisms

Precipitation (along with temperature) is the source and principal control of the spatial distributions of other water resources on the warming TP, with its significant ice, snow, and permafrost cover. Spatially significant changes to other components of the hydrological cycle (*e.g.*, evaporation, glaciers, snow cover, lake volume/area, permafrost, river runoff, and water storage) over the TP appear in good agreement with the patterns of precipitation changes obtained in our study, generally increasing for the central TP and decreasing for regions around the TP (**Fig. 3**, **Figs S1**–**S4**). Precipitation changes and the corresponding unbalanced variations of other water resources over the TP might plausibly have been amplified by coupling and interaction with thermal and dynamic changes in the Arctic and Antarctica, thereby affecting the global climate and water cycles (Wu and Zhang, 1998; Xu *et al*., 2008). The comparatively systematic and uniform patterns of change for each component of the hydrological cycles extant over the TP indicate that large-scale weather or climate systems must play a role in inducing the precipitation or temperature changes that have caused the instability in water-related circulation in our study region.

Fig. 10

We present the large-scale circulation patterns in terms of the divergent wind vector field and specific humidity at the 500-hPa pressure level (panels (a) and (c) in **Fig. 10**), and OLR (panels (b) and (d) in **Fig. 10**) over and around our study area. All proxies are the long term mean over the period 1981–2010. Seasonal (spring, autumn, winter, and annual) circulations are shown as panels (a) and (b) in **Fig. 10**, whereas those in the summer months (June, July, August, and summer averages) are shown separately in panels (c) and (d). The OLR values are negatively correlated with convection (Wang and Xu, 1997) during convective processes in the monsoon seasons (*i.e.*, summer in the TP), while being positively correlated with temperatures in non-monsoon seasons and are widely used for monitoring the earth–atmosphere radiation balance (Gruber and Winston, 1978). Combining the wind vector field and specific humidity at the 500-hPa pressure level with the OLR illustrates the seasonal variability of the large-scale moisture transportation processes in TP. In summer months, humid air (high specific humidity) is transported to the TP along the Indian summer monsoon pathways. The Bay of Bengal and the Indian Peninsula have the lowest OLR values; spatially the OLR increases from southeast to northwest (**Fig. 10**(d4)). Convective processes dominate during the monsoon season, and generally weaken on a trajectory from the origins of the Indian monsoon to the central TP. The wind directions of the Indian summer monsoon to the TP are mainly from the southwest and south (panel (c) in **Fig. 10**), while some shift to southeasterly in the monsoon season and dominate the southern TP (**Fig. 10**(c2), (c4)). The southwesterly, southerly, and southeasterly winds of the Indian summer monsoon pathways to the TP coincide with the southwesterly Dir_{min} based on the 132 CMA stations (panel (a) in **Fig. 4**). Specific humidity in seasons other than summer (panel (a) in **Fig. 10**) is low, with the highest values of ~3 g/kg occurring in northern and western Eurasia. The spatial patterns of OLR in winter ((**Fig. 10**(b3): low in Mongolia and northern China, and increasing from north to south) are clearly consistent with the temperature patterns. In spring (**Fig. 10**(a1)), autumn (**Fig. 10**(a2)), and the annual average (**Fig.**

10(a4)), spatial patterns of specific humidity are similar to those in summer (**Fig. 10**(c4)), but with two areas of extremely low values of specific humidity over the northern TP and the South China Sea. Similar patterns are found in OLR. Combining specific humidity and OLR values (panel (b) in **Fig. 10**), the low OLR values and low specific humidity on the northern TP are related to low temperatures and a weak Indian monsoon, whereas those in the South China Sea correspond to intensive convection. The spatial patterns of large-scale circulation for each season (**Fig. 10**) are consistent with those observed in precipitation trends (**Fig. 3**, **Figs S1**–**S4**, and **Fig. 5**; *i.e.*, increases over the inner TP but decreases over the southern TP), and Dir_{max} or Dir_{min} (panel (a) in **Fig. 4**), in which the Dir_{max} or Dir_{min} in spring, summer, autumn, and the annual average (**Fig. 4**(a1), (a2), (a3), (a5)) are well-organized (with southwesterly Dir_{min}), but are randomly scattered in winter (**Fig. 4**(a4)).

Considering the importance of moisture sources for water cycles, scientists have frequently focused on the quantitative identification of moisture sources over and around the TP using various datasets and analytical methods (Chen *et al*., 2012; Feng *et al*., 2012; Ma *et al*., 2018; Pan *et al*., 2019). Using the High Asia Refined analysis dataset that better represents the complex topography of the TP, Curio *et al.* (2015) presented a 12-year high-resolution climatology of atmospheric water transport. This showed that ~37% of moisture comes from outside the TP, and that the proportion coming from local moisture recycling is ~63%, with no transport from the East Asian monsoon detectable. Zhang C *et al*. (2017) estimated from a modified Water Accounting Model that > 69% of the moisture over the TP comes from the land and 21% from the ocean; they attributed the precipitation increases during the 1979−2013 period to an enhanced southwesterly flux and local moisture supply. The effect of the local moisture supply can be verified using the increased precipitation recycling ratio and a delineation of the effect of intensified hydrological cycles within a warming environment. Pan *et al.* (2019) used the Community Atmospheric Model to demonstrate that the tropical Indian Ocean (central TP) is the dominant supplier of moisture to the southern (northern) TP in the summer. Qi *et al*. (2016) used a topographical model to explain the spatial distribution of precipitation. They asserted that moist southeasterlies from the Bay of Bengal make the greatest contribution (32.56%) to precipitation over the TP, and that moisture sources from the east, south, and west contribute 23.59%, 23.48% and 20.37%, respectively. Although no consistent ratios of different moisture sources over and around the TP have been formulated, the mainstream view appears to be that major moisture sources from the central TP (Indian monsoon) dominate the northwestern (southeastern) TP, and that these differ proportionally during different seasons.

Fig. 11

Local moisture recycling plays an essential role in maintaining an active hydrological cycle (An *et al*., 2017), especially for the central TP, with its higher proportion of locally recycled moisture. Cryosphere melt and water cycle intensification, accompanied by a rapid warming over the TP, have been reported for some time (Yao *et al*., 2012, 2019). Guo and Wang (2014) suggested that, for regions with local water vapor as the major supplier, an intensified local recycling within a warming climatic regime may be responsible for precipitation increases. As calculated by Zhang C *et al*. (2019), moisture from intensified local recycling on the central TP contributes as much as ~52% to the increases in precipitation over recent decades on the northern TP. Based on an analysis of the water budget, Zhang C *et al.* (2017) concluded that the effect of increases in atmospheric moisture and evaporation on changes in precipitation was enhanced because there was more water vapor in the atmosphere and more evaporation produced by the unstable hydrological cycles typical of a warming climate. Thus, the comparatively uniform precipitation increases observed for the central TP in this analysis (**Fig. 3, Figs S1–S4**, **Figs 5–7**) and in previous studies (Yao *et al*., 2013; Deng *et al*., 2017) may result from intensified local recycling and accelerated interaction between atmosphere and the land surface in a warming environment. On the one hand, given the warming background, the equilibrium state in the water resource components of the hydrological cycle will break down, resulting in accelerated glacial retreat, changes in snow cover and permafrost, and enhanced evaporation rates. These processes will contribute to more intense local moisture circulation in the atmosphere, cryosphere, and local ecosystems, further enhancing the instability of local hydrological cycles. On the other hand, a warming climate affects and changes land surface conditions such as vegetation cover changes, glacial retreat, lake expansion, soil moisture content and land surface evaporation, dramatically contributing to changes in both local and regional hydrological cycles.

For the southern TP or regions around the margin of the TP, where the Indian monsoon is the dominant moisture source, variability in the moisture transported to these regions from the tropical Indian Ocean plays a more significant role in precipitation changes, with such variability closely related to the intensity of the Indian monsoon (Stolbova *et al.*, 2016; Mohan and Rajeevan, 2017). Srinivasan (2012) detected a synchronous reduction in the strength of the Indian summer and winter monsoons in the Indian region during periods of Northern Hemisphere cold phase. Using a quasi-isentropic backward trajectory model, decreases in Indian Ocean evaporative sources were reported (Xu *et al*., 2019) and considered as the major factor responsible for the decreases in precipitation observed on the southeastern TP. Upper-air wind speed observed using the rawinsonde method can delineate the intensity of large-scale atmospheric patterns such as the Indian monsoon. Significant reductions in ground level wind speeds over the TP and its surrounding regions have been documented (Yang *et al*., 2014; Guo *et al*., 2017a). Lin *et al*. (2013) observed similar trends in the relation between surface wind speed and upper-air wind speed at 850 hPa as recorded in the Integrated Global Radiosonde Archive, with a correlation coefficient of 0.7, thereby verifying the presence of a weakening Indian monsoon over recent decades over and around the TP. Thus, we attribute the decreases in precipitation for regions around the TP to a weakening Indian monsoon as revealed by a downward trend in wind speeds for both the ground and upper-air measurements.

Spatial patterns of precipitation trends over the Earth's highest plateau and their possible mechanisms are of great importance for understanding hydrological cycles and have therefore attracted scientific attention. Using *P–E* (precipitation–evaporation) to represent changes in moisture sources, Gao *et al*. (2014) revealed a generally wetter climate for the vast northwestern TP, but a drier one for the southeastern TP; they analyzed the poleward shift of the East Asian westerly jet and the poleward transport of moisture, as well as the intensification of summer monsoonal circulation in a warming environment. They concluded that all these factors were responsible for the generally wetter climate experienced by the central TP. Jiang *et al*. (2017) proposed that the dipole pattern of summer rainfall across the Indian subcontinent and the TP is closely associated with anomalies in rainfall, atmospheric circulation and water vapor transport over the Asian continent and the nearby oceans. Wang *et al.* (2017) concluded that multi-year variabilities in southern TP precipitation are mainly controlled by remote moisture transport, as well as a significant impact exerted by the summer North Atlantic Oscillation. Zhou et *al.*

(2019) attributed the interdecadal variabilities evident in the wetting phase observed for summer precipitation over the TP to water vapor changes exported from the eastern margins of the TP, which they suggested were strongly associated with a summer atmospheric circulation anomaly located near Lake Baikal. Sun *et al*. (2020) analyzed the wetting processes in the inner TP and changes in atmospheric circulation over 1979–2018. They found close relations between wetting and the weakened westerlies over the TP, with weakening of the westerlies significantly correlated with the Atlantic multidecadal oscillation on interdecadal scales.

In this analysis, an intensified local recycling from climate warming (the central TP) and a weakening Indian monsoon (southern TP and regions around the TP) are the possible causes of spatial precipitation changes (increases on the central TP and decreases in regions around the TP). For the 16 *Dir*s as shown in **Fig. 4**, we noticed the crossed distributions of positive/negative correlation coefficients between precipitation amounts and W_s values (or temperatures), especially for stations under the combined effect of the Indian monsoon, local moisture circulation and the westerlies (stations in unti-southwestern *Dir*s). Warming of the air, and the consequent intensified or unstable hydrological cycles triggered precipitation increases, while the weakened Indian monsoon has exactly the reverse effect on precipitation trends (precipitation decreases). Over recent decades, the warming of the TP (Qin *et al.*, 2009; Liu *et al.*, 2009; Pepin *et al.*, 2015) and wind weakening (Lin *et al.*, 2013; Guo *et al.*, 2017a) have occurred simultaneously, described as “elevation dependent warming” and “elevation dependent wind weakening”. Results in this analysis indicate that the precipitation changes over the TP are affected by the interaction and battle between a weakening Indian monsoon (decreasing the precipitation) and accelerated local recycling (increasing the precipitation), making our study area’s spatial precipitation trends even more complex. From the CMFD reanalysis (**Figs 5–7**), a general pattern of "central positive and southern/surrounding negative changes" exists, with no distinct boundaries, and this is true for both precipitation trends and precipitation correlations with climate variables (*e.g.*, *Shum*, *Temp*, *Wind*). For stations or precipitation events with higher contributions from locally recycled moisture or from the westerlies (Indian monsoon) moisture sources, more positive correlations were detected between precipitation amount and temperatures (W_s or *Wind*). In the work conducted by Guo *et al*. (2017a), altitude-dependent warming, and thus decreasing horizontal pressure gradients, were suggested as primary causes of near-surface wind speed decreases. Therefore, the positive (or negative) correlations between precipitation and W_s/*Wind* are coincidental, and do not contradict, with the negative (or positive) correlations between precipitation and temperature (*e.g.*, T_{max}, T_{min}, T_{mean}, and *Temp*).

5 Conclusions

The TP has undergone dramatic hydrological changes in recent decades. These changes might have affected the local and regional climate through thermal and dynamic processes. Knowledge of the spatial patterns of precipitation changes over the TP and their possible mechanisms within a warming environment can provide an insight into the instability experienced by hydrological cycles and water resources in the Asian Water Tower region. With this goal, ground-based measurements from 132 CMA stations and the CMFD reanalysis over and around the TP, including precipitation amounts, temperatures (T_{max}, T_{min}, T_{mean}, *Temp*), W_s and winds (W_d and *Wind*) were used. We observed pronounced spatial patterns of precipitation changes throughout the study region that can be generally described as increases on the central

TP and decreases over the southern TP and regions around the TP. Stations with maximum precipitation decreases were mainly controlled by the southwesterly W_d, especially during the spring, summer, autumn, and annually. Positive correlations between averaged precipitation amounts and corresponding temperature (or W_s) values were observed in *Dir*s like Dir_{max} (or Dir_{min}), which were further verified by the positive (or negative) relationships between precipitation and *Temp* (or *Wind*) in regions of the inner TP (avoiding the regions with significant precipitation decreases in the southern TP) from the CMFD reanalysis. We therefore suggest that an intensified local recycling within a warming environment has led to precipitation increases on the central TP, whilst decreased precipitation in the regions surrounding the TP may be attributed to a weakening Indian monsoon as revealed by reductions in both the near-surface and upper-air wind speeds. Issues and caveats such as the spatially uneven distributions of CMA stations, and a paucity of observed measurements for altitudes of >5,000 m asl may limit the quality of the results; the CMFD reanalysis may help refine the gaps. Other possible causes in addition to the warming of the TP (central TP) and a weakening Indian monsoon (the TP's surrounding regions) will be investigated further in future research.

Acknowledgments

This research was funded by the National Natural Science Foundation of China (Grant Nos. 42071090, 41701080, 91747201, 41771043, 41530748, 41571033) and the Strategic Priority Research Program of the Chinese Academy of Sciences (XDA19070301 and XDA20060202). We thank the China Meteorological Administration (CMA, http://data.cma.cn/) and National Tibetan Plateau Data Center (China Meteorological Forcing Dataset, CMFD, http://data.tpdc.ac.cn) for access to

the data used in this analysis. The data that support the findings of this study are available from the CMA (http://data.cma.cn/) and the CMFD (http://data.tpdc.ac.cn).

References:

An, W. L., Hou, S. G., Zhang, Q., Zhang, W. B., Wu, S. Y., Xu, H., Pang, H. X., Wang, Y. T., & Liu, Y. P. (2017). Enhanced Recent Local Moisture Recycling on the Northwestern Tibetan Plateau Deduced From Ice Core Deuterium Excess Records. *Journal of Geophysical Research: Atmospheres*, *122*(23), 12541–12556.

Barreiro, M., & Díaz, N. (2011). Land–atmosphere coupling in El Niño influence over South America. *Atmospheric Science Letters*, *12*(4), 351–355.

Beaugrand, G. (2009). Decadal changes in climate and ecosystems in the North Atlantic Ocean and adjacent seas. *Deep Sea Research Part II: Topical Studies in Oceanography*, *56*(8–10), 656–673.

Beniston, M., Diaz, H. F., & Bradley, R. S. (1997). Climatic change at high elevation sites: An overview. *Climatic Change*, *36*(3–4), 233–251.

Chen, B., Xu, X. D., Yang, S., & Zhang, W. (2012). On the origin and destination of atmospheric moisture and air mass over the Tibetan Plateau. *Theoretical and Applied Climatology*, *110*(3), 423–435.

Chen, X., Long, D., Hong, Y., Zeng, C., & Yan, D. (2017). Improved modeling of snow and glacier melting by a progressive two−stage calibration strategy with GRACE and multisource data: How snow and glacier meltwater contributes to the runoff of the U pper B rahmaputra R iver basin?. *Water Resources Research*, *53*(3), 2431–2466.

Cheng, G., & Wu, T. (2007). Responses of permafrost to climate change and their environmental significance, Qinghai−Tibet Plateau. *Journal of Geophysical Research:*

Earth Surface, *112*(F2).

Cuo, L., Zhang, Y., Wang, Q., Zhang, L., Zhou, B., Hao, Z., & Su, F. (2013). Climate change on the northern Tibetan Plateau during 1957–2009: Spatial patterns and possible mechanisms. *Journal of Climate*, *26*(1), 85–109.

Cuo, L., Zhang, Y., Bohn, T. J., Zhao, L., Li, J., Liu, Q., & Zhou, B. (2015). Frozen soil degradation and its effects on surface hydrology in the northern Tibetan Plateau. *Journal of Geophysical Research: Atmospheres*, *120*(16), 8276–8298.

Curio, J., Maussion, F., & Scherer, D. (2015). A 12-year high-resolution climatology of atmospheric water transport over the Tibetan Plateau. *Earth System Dynamics*, *6*(1), 109–124.

Deng, H., Pepin, N. C., & Chen, Y. (2017). Changes of snowfall under warming in the Tibetan Plateau. *Journal of Geophysical Research: Atmospheres*, *122*(14), 7323–7341.

Diaz, H. F., & Bradley, R. S. (1997). Temperature variations during the last century at high elevation sites. In *Climatic change at high elevation sites* (pp. 21–47). Springer, Dordrecht.

Feng, L., & Zhou, T. (2012). Water vapor transport for summer precipitation over the Tibetan Plateau: Multidata set analysis. *Journal of Geophysical Research: Atmospheres*, *117*(D20).

Gao, Y., Cuo, L., & Zhang, Y. (2014). Changes in moisture flux over the Tibetan Plateau during 1979–2011 and possible mechanisms. *Journal of climate*, *27*(5), 1876–1893.

Gruber, A., Winston, J.S. (1978). Earth-Atmosphere Radiative Heating Based on Noaa Scanning Radiometer Measurements. *Bulletin of the American Meteorological Society*, 59(12), 1570–1573.

Guenette, S., Araujo, J. N., & Bundy, A. (2014). Exploring the potential effects of climate change on the Western Scotian Shelf ecosystem, Canada. *Journal of Marine Systems*, *134*, 89–100.

Guo, Y., & Wang, C. (2014). Trends in precipitation recycling over the Qinghai–Xizang Plateau in last decades. *Journal of hydrology*, *517*, 826–835.

Guo, D., & Wang, H. (2013). Simulation of permafrost and seasonally frozen ground conditions on the Tibetan Plateau, 1981–2010. *Journal of Geophysical Research: Atmospheres*, *118*(11), 5216–5230.

Guo, D., Sun, J., Yang, K., Pepin, N., & Xu, Y. (2019). Revisiting recent elevation−dependent warming on the Tibetan Plateau using satellite−based data sets. *Journal of Geophysical Research: Atmospheres*, *124*(15), 8511–8521.

Guo, X., Wang, L., & Tian, L. (2016). Spatio−temporal variability of vertical gradients of major meteorological observations around the Tibetan Plateau. *International Journal of Climatology*, *36*(4), 1901–1916.

Guo, X., Wang, L., Tian, L., & Li, X. (2017a). Elevation−dependent reductions in wind speed over and around the Tibetan Plateau. *International Journal of Climatology*, *37*(2), 1117–1126.

Guo, X., Tian, L., Wen, R., Yu, W., & Qu, D. (2017b). Controls of precipitation δ18O on the northwestern Tibetan Plateau: A case study at Ngari station. *Atmospheric Research*, *189*, 141–151.

Hrudya, P. H., Varikoden, H., & Vishnu, R. (2020). A review on the Indian summer monsoon rainfall, variability and its association with ENSO and IOD. *Meteorology and Atmospheric Physics*, 1–14.

Immerzeel, W. W., Van Beek, L. P., & Bierkens, M. F. (2010). Climate change will affect the Asian water towers. *Science*, *328*(5984), 1382–1385.

Jiang, X., & Ting, M. (2017). A dipole pattern of summertime rainfall across the Indian subcontinent and the Tibetan Plateau. *Journal of Climate*, *30*(23), 9607–9620.

Jung, M., Reichstein, M., Ciais, P., Seneviratne, S. I., Sheffield, J., Goulden, M. L., Bonan, G., Cescatti, A., Chen, J. Q., de Jeu, R., Dolman, A. J., Eugster, W., Gerten, D., Gianelle, D., Gobron, N., Heinke, J., Kimball, J., Law, B. E., Montagnani, L., Mu, Q. Z., Mueller, B., Oleson, K., Papale, D., Richardson, A. D., Roupsard, O., Running, S., Tomelleri, E., Viovy, N., Weber, U., Williams, C., Wood, E., Zaehle, S., & Zhang, K. (2010). Recent decline in the global land evapotranspiration trend due to limited moisture supply. *Nature*, *467*(7318), 951–954.

Kang, S., Xu, Y., You, Q., Flügel, W. A., Pepin, N., & Yao, T. (2010). Review of climate and cryospheric change in the Tibetan Plateau. *Environmental research letters*, *5*(1), 015101.

Klein, J. A., Harte, J., & Zhao, X. Q. (2004). Experimental warming causes large and rapid species loss, dampened by simulated grazing, on the Tibetan Plateau. *Ecology Letters*, *7*(12), 1170–1179.

Knapp, A. K., Beier, C., Briske, D. D., Classen, A. T., Luo, Y., Reichstein, M., Heisler, J. L. (2008). Consequences of more extreme precipitation regimes for terrestrial ecosystems. *Bioscience*, *58*(9), 811–821.

Kuang, X., & Jiao, J. J. (2016). Review on climate change on the Tibetan Plateau during the last half century. *Journal of Geophysical Research: Atmospheres*, *121*(8), 3979–4007.

Kuttippurath, J., Murasingh, S., Stott, P. A., Sarojini, B. B., Jha, M. K., Kumar, P., Nair, P. J., Varikoden, H., Raj, S., Francis, P. A., & Pandey, P. C. (2021). Observed rainfall changes in the past century (1901–2019) over the wettest place on Earth. *Environmental Research Letters*, *16*(2), 024018.

Lei, Y., Yao, T., Bird, B. W., Yang, K., Zhai, J., & Sheng, Y. (2013). Coherent lake growth on the central Tibetan Plateau since the 1970s: Characterization and attribution. *Journal of Hydrology*, *483*, 61–67.

Li, X., Wang, L., Guo, X., & Chen D. (2017). Does summer precipitation trend over and around the Tibetan Plateau depend on elevation? *International Journal of Climatology*, 37 (S1): 1278–1284.

Lin, C., Yang, K., Qin, J., & Fu, R. (2013). Observed coherent trends of surface and upper-air wind speed over China since 1960. *Journal of Climate*, *26*(9), 2891–2903.

Liu, X., Cheng, Z., Yan, L., & Yin, Z. Y. (2009). Elevation dependency of recent and future minimum surface air temperature trends in the Tibetan Plateau and its surroundings. *Global and Planetary Change*, *68*(3), 164.

Liu, W., Wang, L., Chen, D., Tu, K., Ruan, C., & Hu, Z. (2016). Large-scale circulation classification and its links to observed precipitation in the eastern and central Tibetan Plateau. *Climate Dynamics*, *46*(11–12), 3481–3497.

Ma, Y., Kang, S., Zhu, L., Xu, B., Tian, L., & Yao, T. (2008). Tibetan observation and research platform: Atmosphere–land interaction over a heterogeneous landscape. *Bulletin of the American Meteorological Society*, *89*(10), 1487–1492.

Ma, Y., Lu, M., Chen, H., Pan, M., & Hong, Y. (2018). Atmospheric moisture transport versus precipitation across the Tibetan Plateau: a mini-review and current challenges. *Atmospheric research*, *209*, 50–58.

Mackay, A. (2008). Climate change 2007: impacts, adaptation and vulnerability. Contribution of Working Group II to the fourth assessment report of the Intergovernmental Panel on Climate Change. *Journal of Environmental Quality*, *37*(6), 2407.

Maussion, F., Scherer, D., Mölg, T., Collier, E., Curio, J., & Finkelnburg, R. (2014).

Precipitation seasonality and variability over the Tibetan Plateau as resolved by the High Asia Reanalysis. *Journal of Climate*, *27*(5), 1910–1927.

Mcvicar, T. R., Roderick, M. L., Donohue, R. J., Li, L. T., Van Niel, T. G., Thomas, A., Grieser, J., Jhajharia, D., Himri, Y., & Mahowald, N. M. (2012). Global review and synthesis of trends in observed terrestrial near-surface wind speeds: implications for evaporation. *Journal of Hydrology*, *416*, 182–205.

Meng, F., Su, F., Li, Y., & Tong, K. (2019). Changes in terrestrial water storage during 2003–2014 and possible causes in Tibetan Plateau. *Journal of Geophysical Research: Atmospheres*, *124*(6), 2909–2931.

Mohan, T. S., & Rajeevan, M. (2017). Past and future trends of hydroclimatic intensity over the Indian monsoon region. *Journal of Geophysical Research: Atmospheres*, *122*(2), 896–909.

Mölg, T., Maussion, F., & Scherer, D. (2014). Mid-latitude westerlies as a driver of glacier variability in monsoonal High Asia. *Nature Climate Change*, *4*(1), 68–73.

Nair, P. J., Chakraborty, A., Varikoden, H., Francis, P. A., & Kuttippurath, J. (2018). The local and global climate forcings induced inhomogeneity of Indian rainfall. *Scientific reports*, *8*(1), 1–12.

Pan, C., Zhu, B., Gao, J., Kang, H., & Zhu, T. (2019). Quantitative identification of moisture sources over the Tibetan Plateau and the relationship between thermal forcing and moisture transport. *Climate dynamics*, *52*(1–2), 181–196.

Pepin, N. C., & Lundquist, J. D. (2008). Temperature trends at high elevations: patterns across the globe. *Geophysical Research Letters*, *35*(14).

Pepin, N., Bradley, R. S., Diaz, H. F., Baraer, M., Caceres, E. B., Forsythe, N., Fowler, H., Greenwood, G., Hashmi, M. Z., Liu, X. D., Miller, J. R., Ning, L., Ohmura, A., Palazzi, E., Rangwala, I., Schoner, W., Severskiy, I., Shahgedanova, M., Wang, M. B., Williamson, S. N., Yang, D. Q., & Grp, M. R. I. E. W. (2015). Elevation-dependent warming in mountain regions of the world. *Nature Climate Change*, *5*(5), 424–430.

Pritchard, H. D. (2019). Asia's shrinking glaciers protect large populations from drought stress. *Nature*, *569*(7758), 649–654.

Qi, W. W., Zhang, B. P., Yao, Y. H., Zhao, F., Zhang, S., & He, W. H. (2016). A topographical model for precipitation pattern in the Tibetan Plateau. *Journal of Mountain Science*, *13*(5), 763–773.

Qin, J., Yang, K., Liang, S., & Guo, X. (2009). The altitudinal dependence of recent rapid warming over the Tibetan Plateau. *Climatic Change*, *97*(1–2), 321.

Rajagopalan, B., & Molnar, P. (2013). Signatures of Tibetan Plateau heating on Indian summer monsoon rainfall variability. *Journal of Geophysical Research: Atmospheres*, *118*(3), 1170–1178.

Rangwala, I., Miller, J. R., & Xu, M. (2009). Warming in the Tibetan Plateau: possible influences of the changes in surface water vapor. *Geophysical research letters*, *36*(6).

Ren, J., Jing, Z., Pu, J., & Qin, X. (2006). Glacier variations and climate change in the central Himalaya over the past few decades. *Annals of Glaciology*, *43*, 218–222.

Shen, M., Tang, Y., Chen, J., Zhu, X., & Zheng, Y. (2011). Influences of temperature and precipitation before the growing season on spring phenology in grasslands of the central and eastern Qinghai-Tibetan Plateau. *Agricultural and Forest Meteorology*, *151*(12), 1711–1722.

Shi, Q., & Liang, S. (2013). Characterizing the surface radiation budget over the Tibetan Plateau with ground−measured, reanalysis, and remote sensing data sets: 2. Spatiotemporal analysis. *Journal of Geophysical Research: Atmospheres*, *118*(16), 8921–8934.

Singh, P., & Nakamura, K. (2009). Diurnal variation in summer precipitation over the central Tibetan Plateau. *Journal of Geophysical Research: Atmospheres*, *114*(D20).

Song, C., Huang, B., Richards, K., Ke, L., & Hien Phan, V. (2014). Accelerated lake expansion on the Tibetan Plateau in the 2000s: Induced by glacial melting or other processes?. *Water Resources Research*, *50*(4), 3170–3186.

Srinivasan, M. S. (2012). Synchronous reduction in Indian summer and winter monsoon intensity during the northern hemisphere cold episodes: possible implications on climate modelling. *Current Science*, *103*(12), 1398.

Stolbova, V., Surovyatkina, E., Bookhagen, B., & Kurths, J. (2016). Tipping elements of the Indian monsoon: Prediction of onset and withdrawal. *Geophysical Research Letters*, *43*(8), 3982–3990.

Su, F., Zhang, L., Ou, T., Chen, D., Yao, T., Tong, K., & Qi, Y. (2016). Hydrological response to future climate changes for the major upstream river basins in the Tibetan Plateau. *Global and Planetary Change*, *136*, 82–95.

Sun, J., Yang, K., Guo, W., Wang, Y., He, J., & Lu H. (2020). Why has the inner Tibetan Plateau become wetter sine the mid-1990s? *Journal of Climate*, 33(19), 8507–8522.

Tian, L., Masson−Delmotte, V., Stievenard, M., Yao, T., & Jouzel, J. (2001). Tibetan Plateau summer monsoon northward extent revealed by measurements of water stable isotopes. *Journal of Geophysical Research: Atmospheres*, *106*(D22), 28081–28088.

Tong, K., Su, F., Yang, D., Zhang, L., & Hao, Z. (2014). Tibetan Plateau precipitation as depicted by gauge observations, reanalyses and satellite retrievals. *International Journal of Climatology*, *34*(2), 265–285.

Wang, X. M., Liu, H. J., Zhang, L. W., & Zhang, R. H. (2014). Climate change trend and its effects on reference evapotranspiration at Linhe Station, Hetao Irrigation

District. *Water Science and Engineering*, *7*(3), 250–266.

Wang, Z., Wu, R., Zhao, P., Yao, S. L., & Jia, X. (2019). Formation of snow cover anomalies over the Tibetan Plateau in cold seasons. *Journal of Geophysical Research: Atmospheres*, *124*(9), 4873–4890.

Wang, Z., Duan, A., Yang, S., & Ullah, K. (2017). Atmospheric moisture budget and its regulation on the variability of summer precipitation over the Tibetan Plateau. *Journal of Geophysical Research: Atmospheres*, *122*(2), 614–630.

Wu, G. X., Li, W. P., & Liu, H. (1997). Sensible heating-driving air pump of the Tibetan Plateau and the Asian summer monsoon. Memorial Volume of Prof. Zhao J. Z and Ye D.Z, 116–126.

Wu, G., & Zhang, Y. (1998). Tibetan Plateau forcing and the timing of the monsoon onset over South Asia and the South China Sea. *Monthly weather review*, *126*(4), 913–927.

Xu, X., Lu, C., Shi, X., & Gao, S. (2008). World water tower: An atmospheric perspective. *Geophysical Research Letters*, *35*(20).

Xu, Y., & Gao, Y. (2019). Quantification of evaporative sources of precipitation and its changes in the Southeastern Tibetan Plateau and Middle Yangtze River Basin. *Atmosphere*, *10*(8), 428.

Yang, K., Ye, B., Zhou, D., Wu, B., Foken, T., Qin, J., & Zhou, Z. (2011). Response of hydrological cycle to recent climate changes in the Tibetan Plateau. *Climatic change*, *109*(3–4), 517–534.

Yang, K., Wu, H., Qin, J., Lin, C., Tang, W., & Chen, Y. (2014). Recent climate changes over the Tibetan Plateau and their impacts on energy and water cycle: A review. *Global and Planetary Change*, *112*, 79–91.

Yang, R., Zhu, L., Wang, J., Ju, J., Ma, Q., Turner, F., & Guo, Y. (2017).

Spatiotemporal variations in volume of closed lakes on the Tibetan Plateau and their climatic responses from 1976 to 2013. *Climatic Change*, *140*(3–4), 621–633.

Yao, T. D., Thompson, L., Yang, W., Yu, W. S., Gao, Y., Guo, X. J., Yang, X. X., Duan, K. Q., Zhao, H. B., Xu, B. Q., Pu, J. C., Lu, A. X., Xiang, Y., Kattel, D. B., & Joswiak, D. (2012). Different glacier status with atmospheric circulations in Tibetan Plateau and surroundings. *Nature climate change*, *2*(9), 663–667.

Yao, T. D., Masson-Delmotte, V., Gao, J., Yu, W. S., Yang, X. X., Risi, C., Sturm, C., Werner, M., Zhao, H. B., He, Y., Ren, W., Tian, L. D., Shi, C. M., & Hou, S. G. (2013). A review of climatic controls on δ18O in precipitation over the Tibetan Plateau: Observations and simulations. *Reviews of Geophysics*, *51*(4), 525–548.

Yao, T. D., Xue, Y. K., Chen, D. L., Chen, F. H., Thompson, L., Cui, P., Koike, T., Lau, W. K. M., Lettenmaier, D., Mosbrugger, V., Zhang, R. H., Xu, B. Q., Dozier, J., Gillespie, T., Gu, Y., Kang, S. C., Piao, S.L., Sugimoto, S., Ueno, K., Wang, L., Wang, W. C., Zhang, F., Sheng, Y. W., Guo, W. D., Ailikun, Yang, X. X., Ma, Y. M., Shen, S. S. P., Su, Z. B., Chen, F., Liang, S. L., Liu, Y. M., Singh, V. P., Yang, K., Yang, D. Q., Zhao, X. Q., Qian, Y., Zhang, Y., & Li, Q. (2019). Recent Third Pole's rapid warming accompanies cryospheric melt and water cycle intensification and interactions between monsoon and environment: Multidisciplinary approach with observations, modeling, and analysis. *Bulletin of the American Meteorological society*, *100*(3), 423–444.

Yin, Y., Wu, S., & Zhao, D. (2013). Past and future spatiotemporal changes in evapotranspiration and effective moisture on the Tibetan Plateau. *Journal of Geophysical Research: Atmospheres*, *118*(19), 10850–10860.

You, Q., Kang, S., Aguilar, E., & Yan, Y. (2008). Changes in daily climate extremes in the eastern and central Tibetan Plateau during 1961–2005. *Journal of Geophysical*

Research: Atmospheres, *113*(D7).

Zhang, C., Tang, Q., & Chen, D. (2017). Recent changes in the moisture source of precipitation over the Tibetan Plateau. *Journal of Climate*, *30*(5), 1807–1819.

Zhang, C., Tang, Q., Chen, D., van der Ent, R. J., Liu, X., Li, W., & Haile, G. G. (2019). Moisture source changes contributed to different precipitation changes over the northern and southern Tibetan Plateau. *Journal of Hydrometeorology*, *20*(2), 217–229.

Zhang, G., Yao, T., Xie, H., Kang, S., & Lei, Y. (2013). Increased mass over the Tibetan Plateau: From lakes or glaciers?. *Geophysical Research Letters*, *40*(10), 2125–2130.

Zhang, G. Q., Yao, T. D., Shum, C. K., Yi, S., Yang, K., Xie, H. J., Feng, W., Bolch, T., Wang, L., Behrangi, A., Zhang, H. B., Wang, W. C., Xiang, Y., & Yu, J. Y. (2017). Lake volume and groundwater storage variations in Tibetan Plateau's endorheic basin. *Geophysical Research Letters*, *44*(11), 5550–5560.

Zhang, T., Zhang, Y. S., Gun, Y. H., Ma, N., Dai, D., Song, H. T., Qu, D. M., & Gao, H. F. (2019). Controls of stable isotopes in precipitation on the central Tibetan Plateau: A seasonal perspective. *Quaternary international*, *513*, 66–79.

Zhang, W., Zhou, T., & Zhang, L. (2017). Wetting and greening Tibetan Plateau in early summer in recent decades. *Journal of Geophysical Research: Atmospheres*, *122*(11), 5808–5822.

Zhang, X., Ren, Y., Yin, Z. Y., Lin, Z., & Zheng, D. (2009). Spatial and temporal variation patterns of reference evapotranspiration across the Qinghai−Tibetan Plateau during 1971–2004. *Journal of Geophysical Research: Atmospheres*, *114*(D15).

Zhang, Y., Huang, W., & Zhong, D. (2019). Major Moisture Pathways and Their Importance to Rainy Season Precipitation over the Sanjiangyuan Region of the

Tibetan Plateau. *Journal of Climate*, *32*(20), 6837–6857.

Zheng, D., Zhang, Q. S., & Wu, S. H. (2000). *Mountain geoecology and sustainable development of the Tibetan Plateau* (Vol. 57). Springer Science & Business Media.

Zhou, C., Zhao, P., & Chen, J. (2019). The Interdecadal Change of Summer Water Vapor over the Tibetan Plateau and Associated Mechanisms. *Journal of Climate*, *32*(13), 4103–4119.

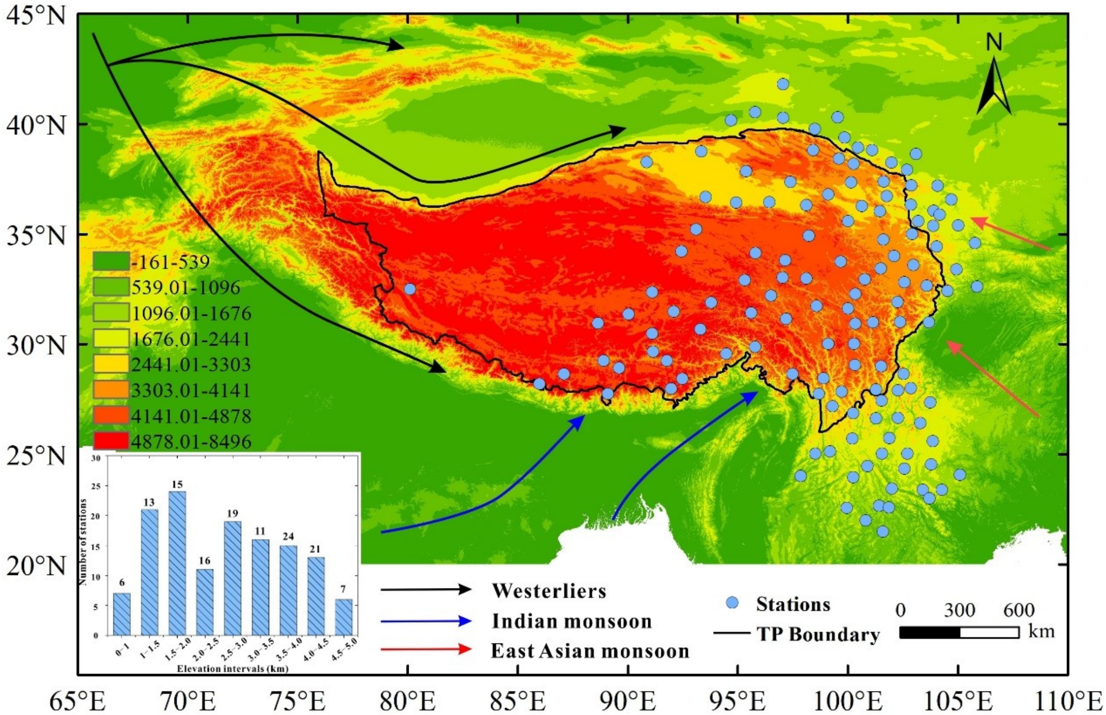

Fig. 1 Locations of the 132 meteorological stations used in this analysis over the Tibetan Plateau (TP), with the diagram in the lower left showing the numbers of stations for each altitudinal band; *i.e.*, <1,000 m asl (above sea level), 1,001–1,500 m asl, 1,501–2,000 m asl, 2,001–2,500 m asl, 2,501–3,000 m asl, 3,001–3,500 m asl, 3,501–4,000 m asl, 4,001–4,500 m asl and 4,501–5,000 m asl. Colored arrows show the usual moisture transport pathways surrounding the TP, including the westerlies (black), the Indian monsoon (blue) and the East Asian monsoon (red). The general topography issued by the Shuttle Radar Topography Mission is shown by color shading.

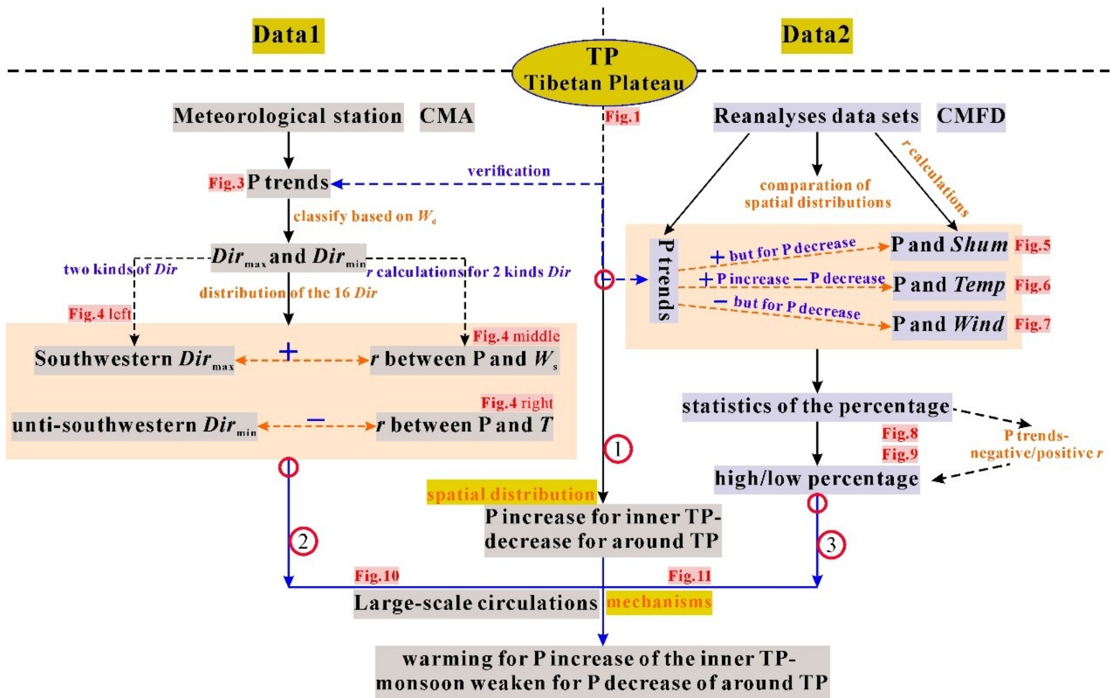

Fig. 2 Framework of this study. Data1 consists of the ground-based observations from the 132 CMA (China Meteorological Administration) stations. Data2 consists of the CMFD (China meteorological forcing dataset) reanalysis. TP is the Tibetan Plateau, P is precipitation, and "W_s" and "T" represent the speed of daily maximum winds, and temperatures from the CMA. *Dir* is direction; Dir_{max} and Dir_{min} are directions of maximum and minimum precipitation changes. "*Shum*" "*Temp*" "*Wind*" are the specific humidity, temperature, and wind speeds from the CMFD, respectively. "r" represents negative or positive linear correlations between precipitation and the controlling factors (*e.g.*, W_s, T, *Shum*, *Temp*, *Wind*).

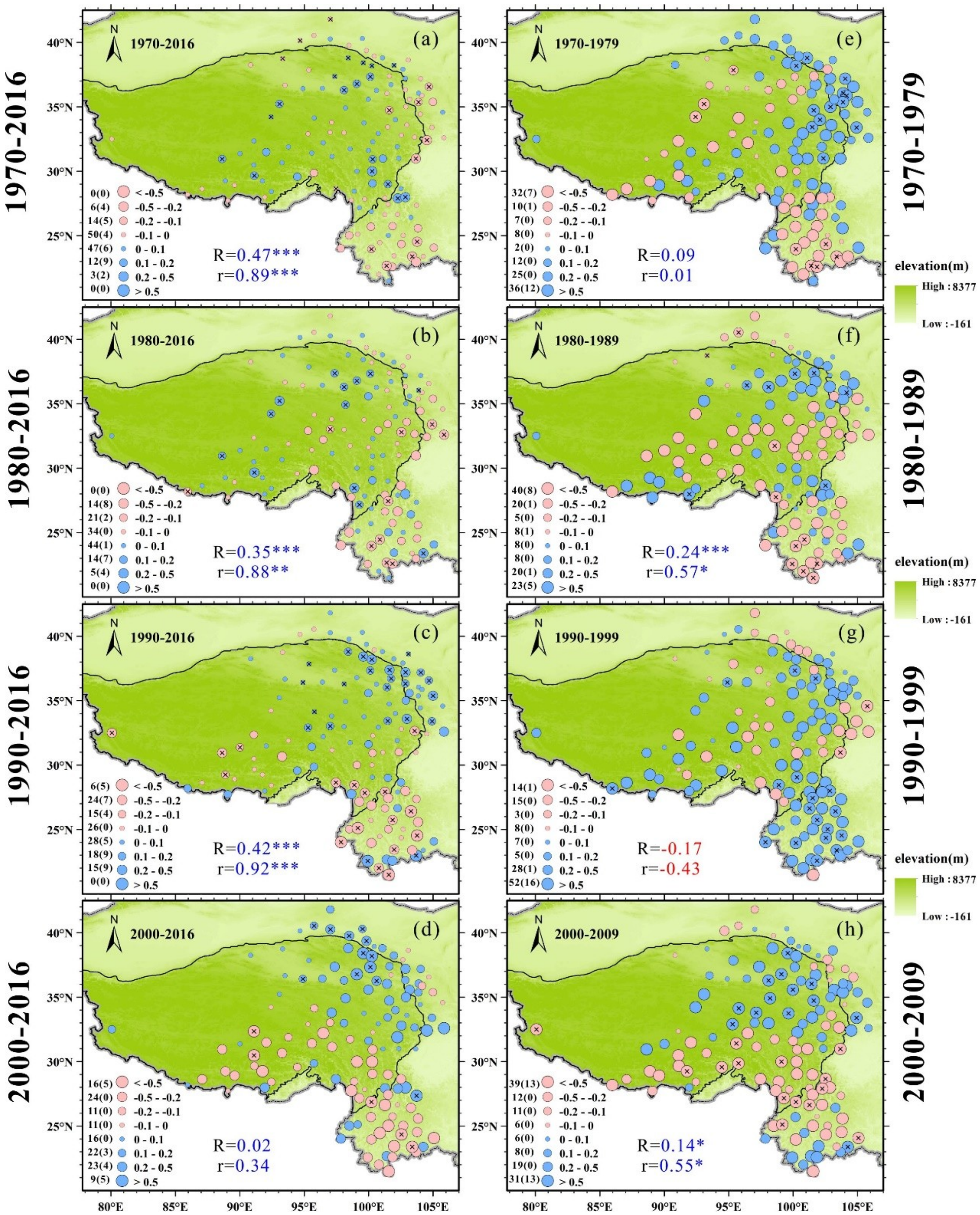

Fig. 3 Trends (mm/10 y) of summer precipitation during each sub-period of the 1970–2016 timeframe (a, 1970–2016; b, 1980–2016; c, 1990–2016; d, 2000–2016; e, 1970–1979; f, 1980–1989; g, 1990–1999; h, 2000–2009) for 132 meteorological stations over the TP. The colored circles show increasing (blue) or decreasing (red) summer precipitation trends; circles with crosses are for values significant at $p < 0.1$. The

numbers beside the differently-sized circles in the lower left represent numbers of stations for each band in decreasing/increasing precipitation trends, while the numbers in brackets represent the numbers of stations where precipitation trends are significant at $p < 0.1$. “R” or “r” are the positive (blue) or negative (red) linear regression coefficients between precipitation changing rates and corresponding altitudes asl for each study period within the 1970–2016 timeframe (“R” represents all the 132 stations, while “r” is obtained from the mean values for each altitudinal band (*i.e.*, <1,000 m asl, 1,001–1,500 m asl, 1,501–2,000 m asl, 2,001–2,500 m asl, 2,501–3,000 m asl, 3,001–3,500 m asl, 3,501–4,000 m asl, 4,001–4,500 m asl and 4,501–5,000 m asl), and */**/*** represent R/r those significant at $p < 0.1$, $p < 0.05$, and $p < 0.01$, respectively.

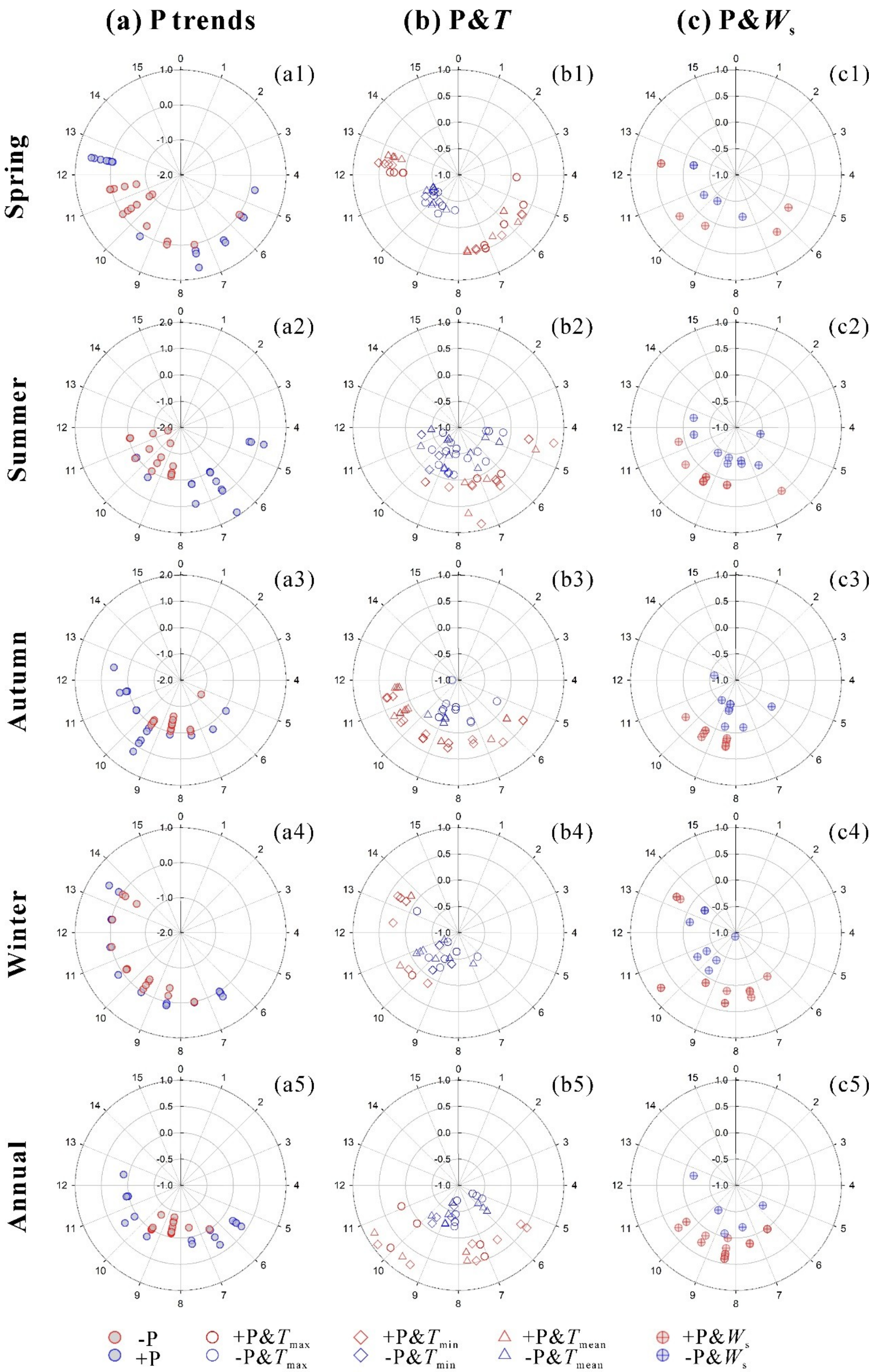
(a) P trends
(b) P&T
(c) P&Ws
Spring
Summer
Autumn
Winter
Annual
(a1)
(b1)
(c1)
(a2)
(b2)
(c2)
(a3)
(b3)
(c3)
(a4)
(b4)
(c4)
(a5)
(b5)
(c5)
-P
+P
+P&Tmax
-P&Tmax
+P&Tmin
-P&Tmin
+P&Tmean
-P&Tmean
+P&Ws
-P&Ws

Fig. 4 (a) Maximal and minimal precipitation trends (mm/10 y), selected from mean values for each of the 16 directions (1−16) based on directions of daily maximum wind speed (W_d) of the 132 stations; (b) linear correlation coefficients of precipitation amount (P) against air temperatures (T: T_{max}, T_{min}, and T_{mean}); and (c) linear correlation coefficients of P against W_s (daily maximum wind speed). Statistics for all the 132 stations, in addition to those stations with P trends significant at $p < 0.1$, for the various study periods within the 1970−2016 timeframe (*i.e.*, 1970−2016, 1980−2016, 1990−2016, 2000−2016, 1970−1979, 1980−1989, 1990−1999 and 2000−2009), are all included in (a). Climate variables (P, T and W_s) used in (b) and (c) are the values for each of the directions in (a). Coefficients of <0.1 (absolute value) are not included in (b) and (c). Colored symbols represent the positive/negative correlations, *i.e.*, circles in (a) with a gray background show positive (blue) or negative (red) P trends, and red (blue) symbols in (b) and (c) represent positive (negative) correlations. The compass points "1–4" correspond to northeast W_d, "5–8" to southeast, "9–12" to southwest and "13–16" to northwest. The four seasons are defined as: spring (November−February), summer (March−May), autumn (June−August) and winter (September−November).

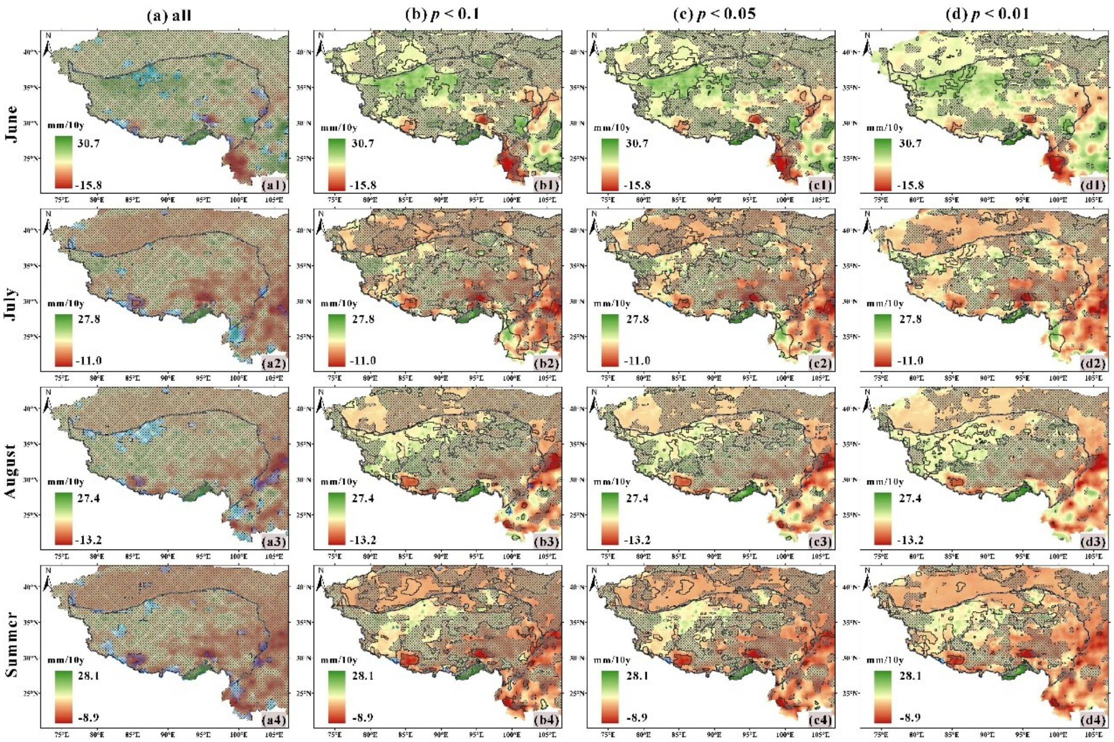

Fig. 5 Rates of recently precipitation changes (mm/10 y, color shading) and correlation coefficients between precipitation (P) and *Shum* (specific humidity, kg/kg, colored crosses) from CMFD reanalysis over the TP during periods 1980–2016. The black bold lines are the TP boundary. Thin black lines show the boundaries for those grid cells with P changes at various significance levels ($p < 0.1$, $p < 0.05$, and $p < 0.01$); colored crosses represent positive (black) or negative (blue) correlations between P and *Shum*. The significance levels are: all grid cells counted, panel (a) , ; $p < 0.1$, panel (b); $p < 0.05$, panel (c); and $p < 0.01$, panel (d). Values are calculated for June, July, August, and the summer period (June to August).

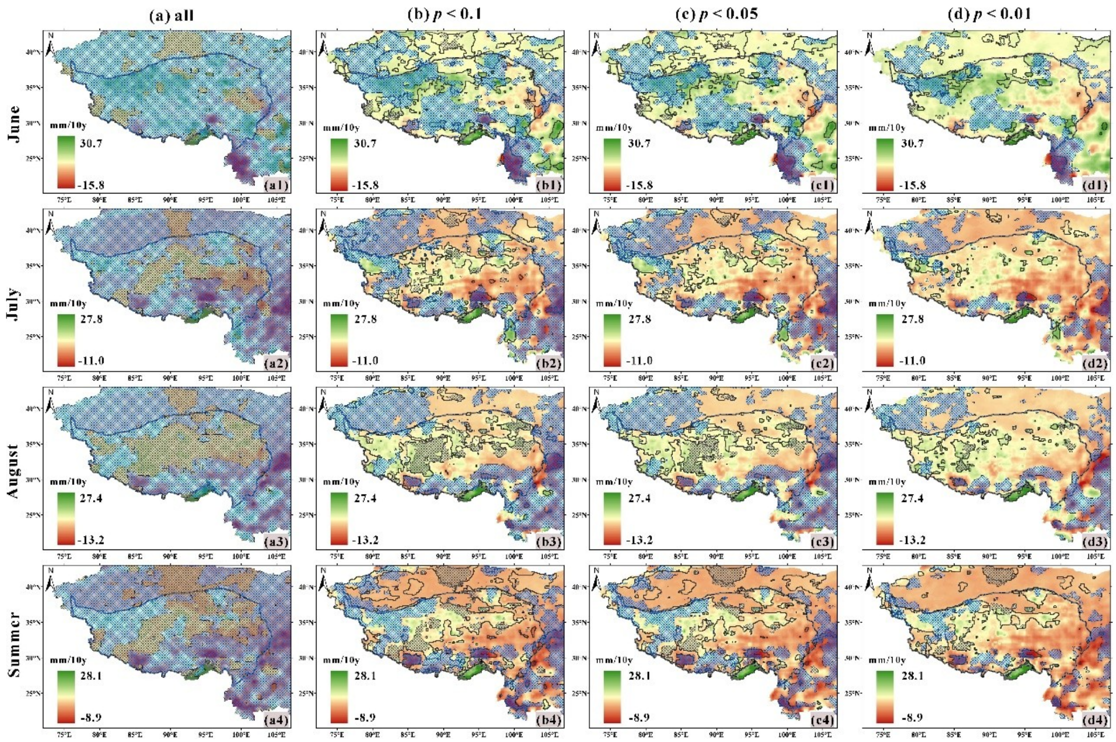

Fig. 6 Same as **Fig. 5**, but for correlations with temperature (*Temp*).

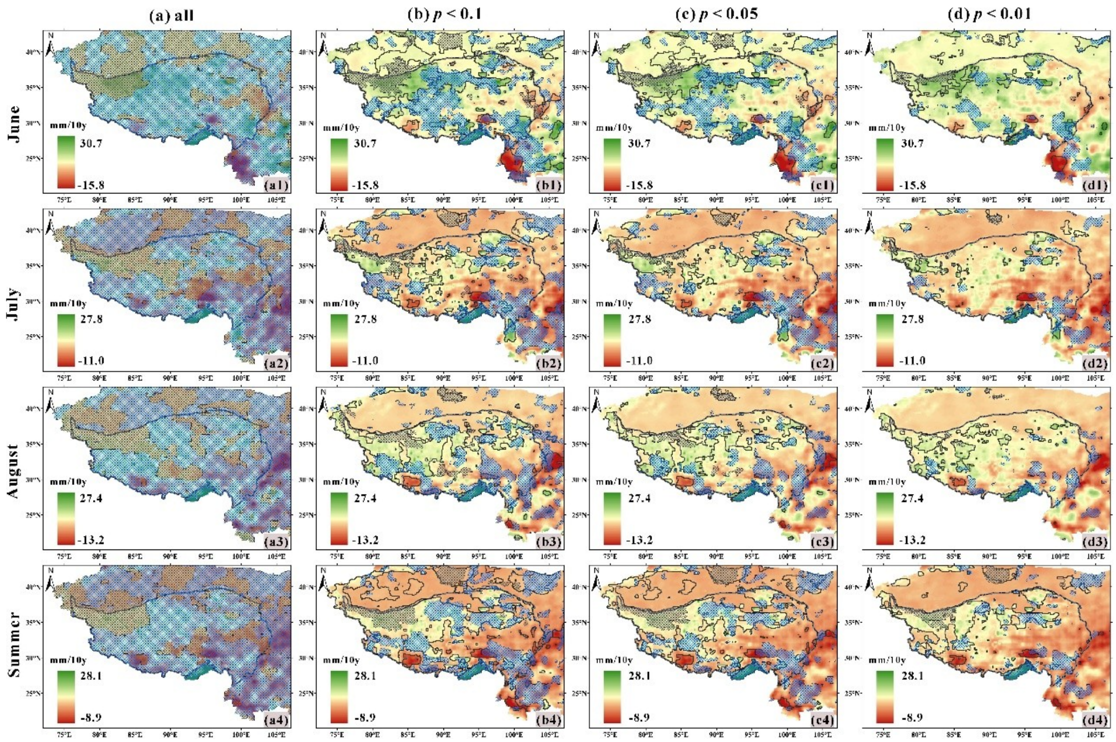

Fig. 7 Same as **Fig. 5**, but for correlations with the near-surface wind speed (*Wind*).

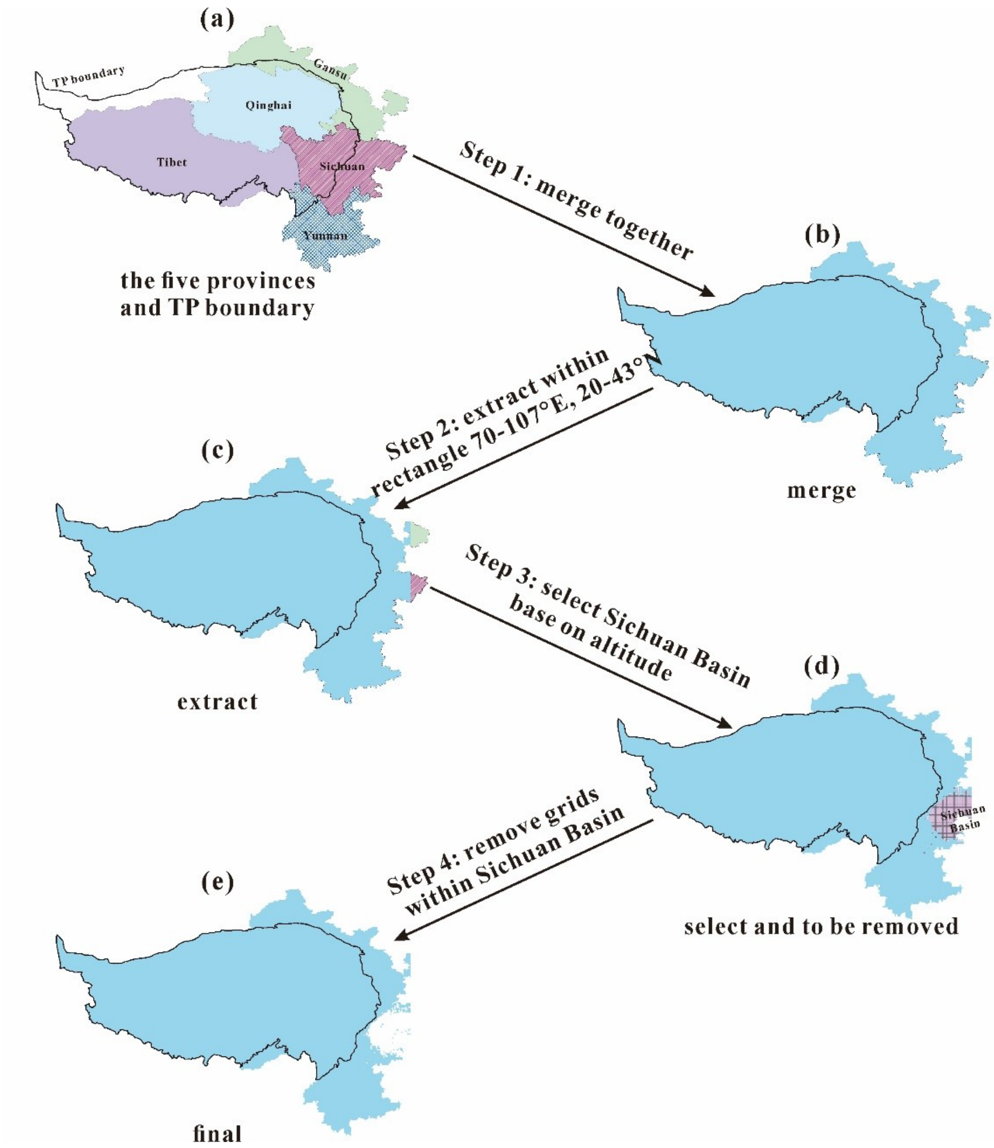

Fig. 8 General steps for generation of the ranges of grid cells to be used in **Fig. 9**. We selected grid cells including the five provinces in western China (*i.e.*, Tibet, Qinghai, Gansu, Yunnan, and Sichuan, colored background in (a)) and within the TP boundary (black lines), while we removed the grid cells outside the rectangle 20–43°N, 78–107°E; grid cells in the Sichuan Basin (<700 m asl and within Sichuan province) are removed for possible disturbance from microtopography. The final area used for ratio calculations in **Fig. 9** is shown in (e), which is consistent with the spatial distribution of the 132 CMA stations.

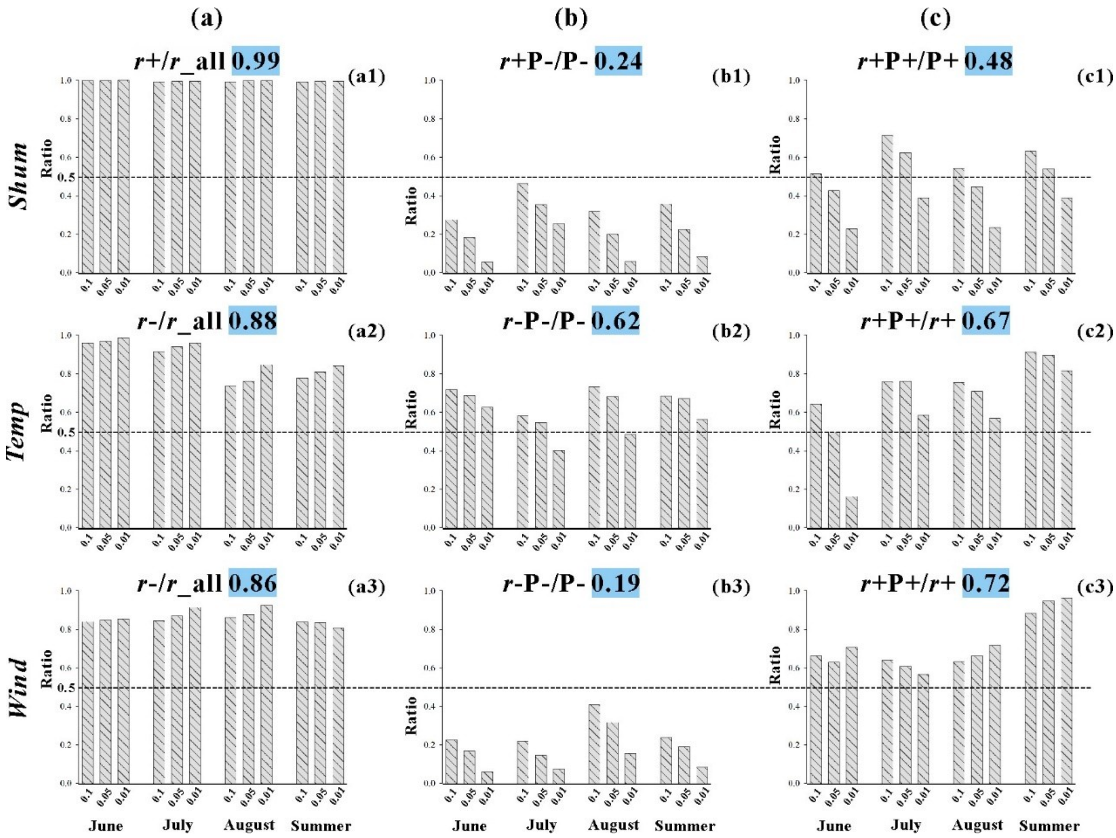

Fig. 9 Statistics for various ratios between positive or negative precipitation trends (P−/P+) and positive or negative correlation coefficients (*r*+/*r*−) between precipitation and *Shum* (specific humidity), *Temp* (temperature) and *Wind* (wind speed) from the CMFD reanalysis in summer months. The exact area of grid cells included is shown in **Fig. 8**. P is precipitation; "*r*" represents correlations between P and *Shum*/*Temp*/*Wind*. Negative or positive trends or correlations are shown by symbols "+" or "−" respectively. "*r*_all" means all the correlations at a certain confidence level. Thus, for example, "*r*+P−/P−" means the ratios of all cells in which P decreased between 1980 and 2016 that also had a positive correlation with certain climatic variables. Numbers with blue background are the averages for each sub-figure.

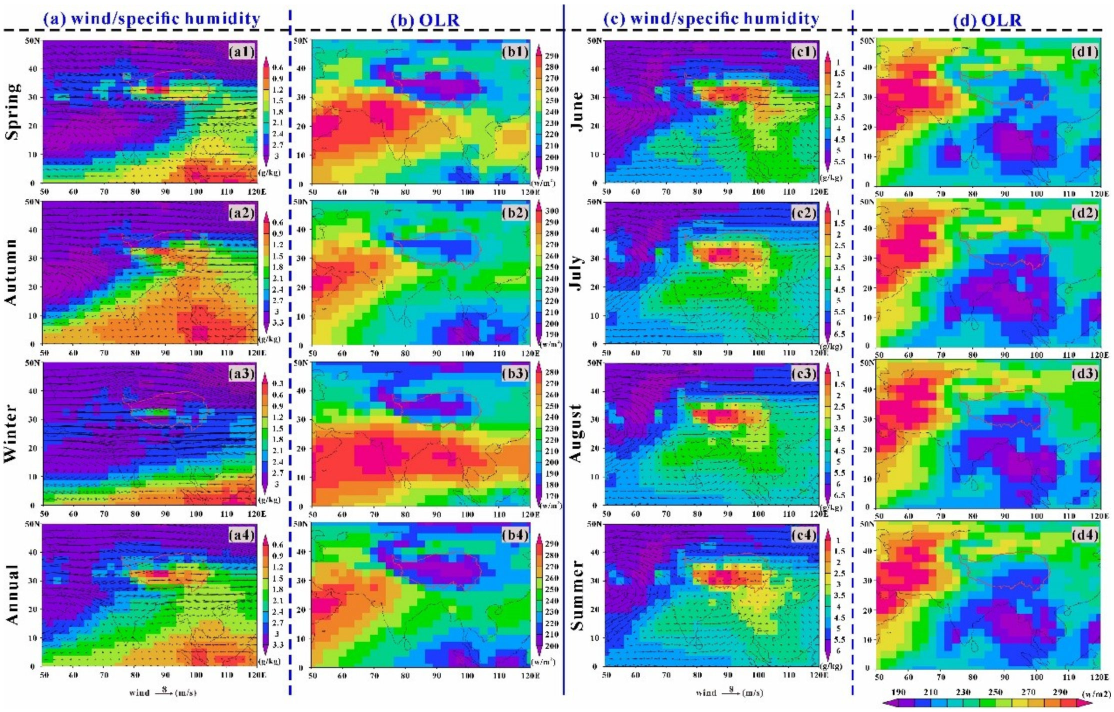

Fig. 10 Wind vector field and specific humidity at 500-hPa pressure level (panels (a) and (c)), and OLR (outgoing longwave radiation; panels (b) and (d)) for each season (panels (a) and (b), spring, autumn, winter, and annual) and in summer months (panels (c) and (d), June, July, August, and summer averages). All values are averaged over periods 1981–2010. The scale for the divergent wind vector field (m/s) is shown at the bottom and the color bar represents specific humidity (g/kg) or radiation (W/m^2). The four seasons are defined as: spring (March–May), summer (June–August), autumn (September–November), and winter (December–February).

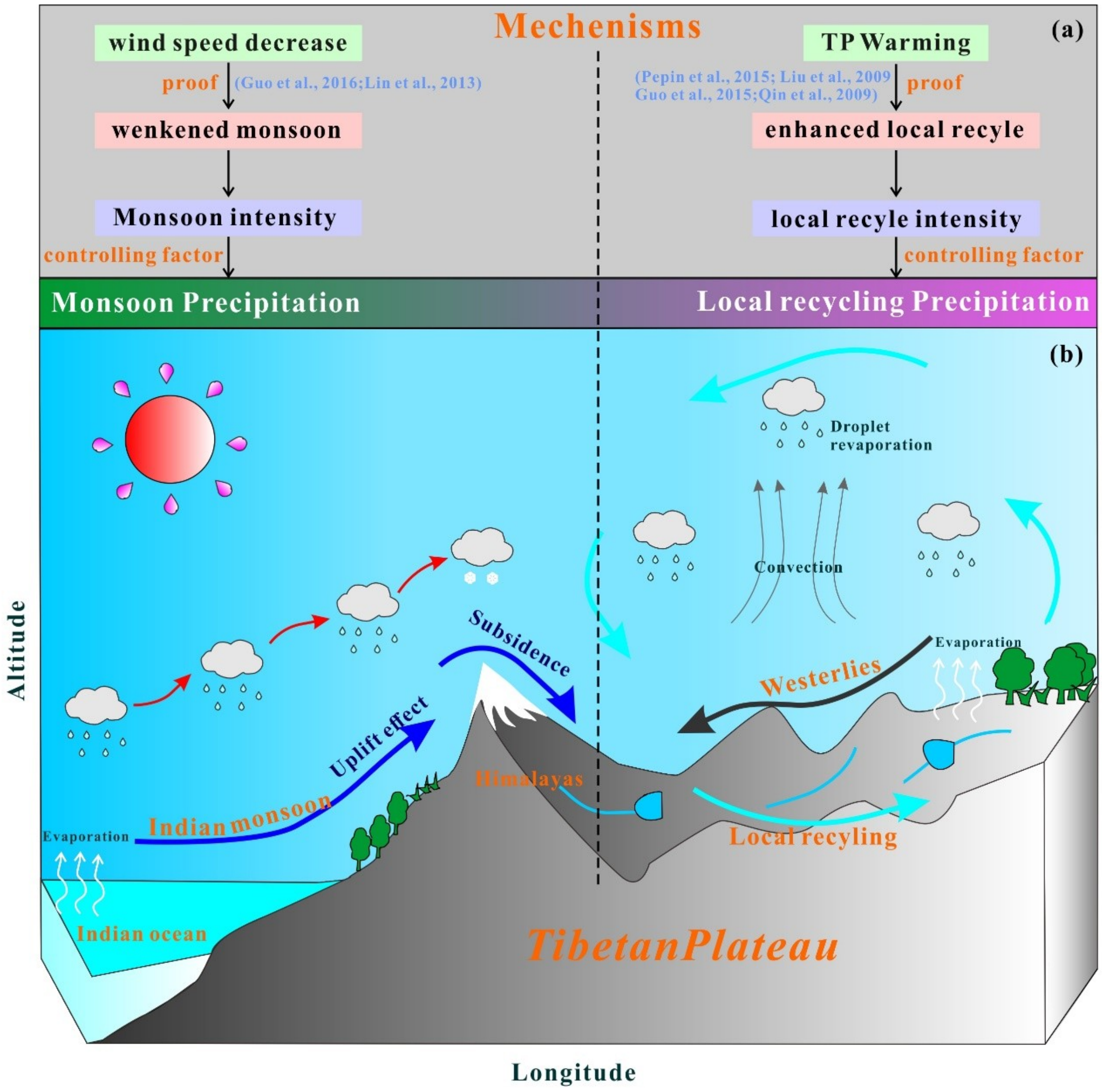

Fig. 11 (a) Possible mechanisms driving the spatial patterns of precipitation changes, which differ between regions surrounding the TP and the central TP; and (b) schematic representation of the main processes affecting recently precipitation change patterns over the TP (with reference to Yao *et al*., 2013).

Table 1. List of variables and abbreviations used in this analysis and their definitions.

Abbreviations	Meanings
TP	the Tibetan Plateau
DEM	the digital elevation model
CMA	the China Meteorological Administration
CMFD	the China Meteorological Forcing Dataset
asl	above sea level
agl	above ground level
P	precipitation
T	temperature from the CMA
T_{max}	daily maximum temperature
T_{min}	daily minimum temperature
T_{mean}	daily mean temperature
W_s	daily maximum wind speed
W_d	directions of daily maximum wind speed
Shum	specific humidity from the CMFD
Temp	temperature from the CMFD
Wind	wind speeds from the CMFD
Dir	directions
Dir_{max}	W_d of maximum precipitation changes
Dir_{min}	W_d of minimum precipitation changes
OLR	outgoing longwave radiation
r	linear correlation coefficients

Table 2. General steps of the recently spatial precipittaion analysis over the Tibetan Plateau, based on datasets of the China Meteorological Administration (CMA) and the China Meteorological Forcing Dataset (CMFD) reanalysis.

CMA		CMFD	
Steps	Figures	Steps	Figures
P trends	3, S1–S4	P trends	5–7
Classification of P trends based on W_d	4(a)	-	-
Correlations of P and W_s/T	4(b), 4(c)	Correlations of P and *Shum*/*Temp*/*Wind*	5–7
Comparative analysis for Dir_{max} and Dir_{min}	4	Comparations for the above spatial distributions	5–7
-	-	Quantitative ratio calculations	8, 9
Possible mechanisms of spatially P trends	11		

P: precipitation;

W_d: directions of daily maximum wind speed;

W_s: daily maximum wind speed;

T: records of temperature from the CMA;

Dir_{max}/Dir_{min}: W_d of maximum/minimum precipitation changes;

Shum/*Temp*/*Wind*: the near-surface specific humidity, temperature, and wind speed from the CMFD reanalysis.

Table 3. Linear correlation coefficients of recent precipitation trends against corresponding altitude over the Tibetan Plateau.

	1970−2016	1980−2016	1990−2016	2000−2016	1970−1979	1980−1989	1990−1999	2000−2009
Spring	0.50***	0.27***	0.44***	0.40***	0.39***	0.17**	0.36***	0.25***
	0.93***	0.71**	0.93***	0.89***	0.82***	0.53	0.75***	0.78***
Summer	0.47***	0.35***	0.42***	0.02	0.09	0.24***	−0.17	0.14*
	0.89***	0.88***	0.92***	0.34	0.01	0.57*	−0.43	0.55*
Autumn	0.31***	0.25***	0.09	0.11	−0.18	0.02	0.08	0.22***
	0.88***	0.78***	0.41	0.56	−0.82	0.22	0.61*	0.81***
Winter	0.000	−0.17*	−0.11	−0.15*	0.31***	0.41***	0.28***	0.18**
	0.11	−0.65*	−0.60*	−0.62*	0.79**	0.94***	0.91***	0.34
annual	0.58***	0.42**	0.44***	0.21**	0.20**	0.29***	0.14*	0.29***
	0.96***	0.96***	0.95***	0.57*	0.21	0.57*	0.73**	0.85***

*/**/*** represent correlations significance at $p < 0.1$, $p < 0.05$ and $p < 0.01$, respectively.

Numbers with a gray background are the coefficients regressed from mean values (precipitation and altitude) with 500 m as their altitudinal interval (< 1,000 m asl, 1,000−1,500 m asl, 1,501−2,000 m asl, 2,001−2,500 m asl, 2,501−3,000 m asl, 3,001−3,500 m asl, 3,501−4,000 m asl, 4,001−4,500 m asl, 4,501−5,000 m asl).

Black and red numbers are positive and negative correlation coefficients, respectively.

The four seasons were defined as: Spring (March−May), Summer (June−August), Autumn (September−November) and Winter (December−February).